TAMPEREEN TEKNILLINEN YLIOPISTO
TAMPERE UNIVERSITY OF TECHNOLOGY

ANTONIO MORENO ORDÓÑEZ

FORCE CONTROLLED PIEZOELECTRIC FIBER PRESS

Master's thesis

Examiner: Professor Pasi Kallio

Examiner and topic approved by the Faculty Council of the Faculty of Automation, Mechanical and Materials Engineering on 05.09.2012.

Abstract

TAMPERE UNIVERSITY OF TECHNOLOGY
Erasmus Programme
MORENO ORDÓÑEZ, ANTONIO: Force Controlled Piezoelectric Fiber Press
Master of Science Thesis, 82 pages, 6 Appendix pages
September 2012
Major subject: Automation Science
Examiner: Professor Pasi Kallio
Keywords: piezoelectric, microsystems, actuator, force control, open-loop control.

The study of the properties of paper in in the micro scale requires the use of devices on the same dimensional order. Paper fiber bonds, the construction unit of paper sheets, can be manufactured, manipulated and tested thanks to a variety of micro actuators. In the manufacturing process of paper fiber bonds, a tool able to press the fibers together is paramount, along with a force control scheme that can guarantee an acceptable performance from the actuator in question.

This thesis proposes an open-loop force control technique for a piezoelectric stack actuator, consisting of the compensation of the hysteresis and creep nonlinearities and vibrations. The hysteresis compensation is based on model inversion, resorting to the Prandtl-Ishlinskii method for modeling static hysteresis. Creep compensation, on the other hand, consists of an inverse multiplicative structure, meaning that no model inversion is required and therefore simplifying the process. Last, vibration is dealt with by means of an input shaping technique.

The thesis starts with a literature study, followed by the discussion of the method to be implemented and the selection of the required software and hardware for the experiments, as well as the design of a custom-built test platform. The second half of the thesis begins with the characterization of the actuator and tackles the design and implementation of the control.

The experimental results show that an open-loop control scheme is possible for force control of a piezoelectric actuator and proves its efficiency and convenience for micromanipulation tasks: hysteresis is reduced to less than 3 %, creep is kept under 1 % and overshoot is decreased to less than 10 % at low inputs and apparently eliminated at higher inputs. Also, the results suggest that this method can easily be extended to other types of actuators and applications, albeit certain additional issues might have to be taken into consideration.

Preface

I would like to start by acknowledging the financial support provided by the European Commission (EC), the Spanish Education Ministry and the Community of Madrid through the Erasmus Programme. On a related note, I would also like to thank the Tampere University of Technology (TUT) for accepting me as an exchange student and offering their facilities to complete my last year of studies and my thesis work.

My deepest gratitude goes to my tutor, Professor Pasi Kallio, for offering me the possibility to carry out my thesis work in the Micro- and NanoSystems Research (MST) Group and providing the foundation I needed to work and lean on.

Same goes to my supervisor, Pooya Saketi, who was always ready to give a hand and, among many things, helped me with the design of the test platform.

I truly appreciate the help of Heikki Huttunen, Antti Vehkaoja and Tery Caisaguano Vásquez with the filtering and amplification of the signal provided by the load cell used in the measurements.

Let us not forget about the rest of the personnel of the MST Group, who helped make the department an enjoyable place to work in. I would like to extend a big thank you to Mathias von Essen, Juha Hirvonen, Joose Kreutzer and Antti Mäki for their help with the different hardware and software-related difficulties I faced during the execution of the experiments and helping me solve several doubts.

And last but not least, I would like to wholeheartedly thank my family, friends and girlfriend for supporting me in every way during my stay in Finland for almost a year.

Madrid, Spain
August 2012

Antonio Moreno Ordóñez

Table of Contents

List of Symbols and Abbreviations

Symbols

A_i	amplitude of the impulse
C	capacitance
$C(s)$	creep transfer function
d	deadzone of the one-sided deadzone operator
d_i	ith deadzone of the one-sided deadzone operator
ΔH	full output range
Δh	maximum difference between output readings for a given input point
E	error
F	force output
F_c	hysteretic, creeped force
f_{cutoff}	cutoff frequency
F_f	final value of the force after a given period of time
F_{fv}	constant part of the hysteretic, creeped force
F_h	hysteretic force
F_i	ith force impulse
F_p	peak value of the force
F_r	reference force
F_{ss}	steady-state value of the force
G	gain of the resistor
H	Prandtl-Ishlinskii hysteresis operator

H_{r_i}	i[th] backlash operator
K_c	static gain of a creeped, badly damped system
K_v	static gain of a badly damped system
n	number of backlash operators
n_s	number of samples
m	number of one-sided deadzone operators
ξ	damping ratio
p	number of impulses in the ZV input shaper
r	deadband or threshold value of the backlash operator
R_G	gain resistance
r_i	i[th] deadband or threshold value of the backlash operator
R_{out}	output resistance
S_{d_i}	i[th] one-sided deadzone operator
T	period
t_i	time delay
T_s	sampling period
w_{h_i}	weight of the i[th] backlash operator
w_n	natural frequency
w_{s_i}	weight of the i[th] one-sided deadzone operator
x	input/output to the direct/inverse PI hysteresis model
y	intermediate input/output to the direct and inverse PI hysteresis models
z	input/output to the inverse/direct PI hysteresis model

Abbreviations

A/D	analog to digital

AC	alternate current
DC	direct current
GUI	graphical user interface
IDE	integrated development environment
Max	maximum
MST Group	Micro- and Nanosystems Research Group at TUT
Min	minimum
PI	proportional and integral
PI method/model	Prandtl-Ishlinskii method/model
PID	proportional, integral and derivative
ZV	zero voltage

1. Introduction

In the ever increasing tendency towards miniaturization of technology in general, piezoelectric actuators have been proven to be useful in micromanipulation applied to a variety of fields. Micromanipulation has made possible, among other things, the study of paper fibers with the objective of gaining a better understanding of the bonds between them and finding ways to improve paper in general.

A piezoelectric stack has been provided in order to press paper fibers together and therefore create paper fiber bonds, as well as to carry out compression tests on paper fibers which will provide important information on the strength of the bonds. The goal of this thesis work is to devise a force control method for the piezoelectric stack and test its performance. Since force control in the micro scale tends to pose a series of complications when resorting to classical control techniques, an alternative approach will be considered.

The introductory chapter consists of three sections. Section 1.1 describes the motivation behind the thesis work. Section 1.2 introduces the objective of the thesis. Finally Section 1.3 will list and shortly describe the rest of the chapters comprising the thesis.

1.1. Motivation of the Thesis

Micromanipulation involves the manipulation of elements with sizes that range from one micrometer to a few millimeters [21]. Over the last few decades micromanipulation has found its application in different fields, such as in biological research and microassembly, thanks to the possibility to handle artificial objects, such as microscopic gears and other components, and natural objects, such as cells, bacteria and, our subject of interest, paper fiber bonds.

The strength of paper is derived from the strength of single fibers and the bonds formed between fibers. Thus, the properties of the individual fiber bonds will determine those of the entire network of a paper sheet. Some research has been done on the properties of fiber bonds, such as [22], which deals with the measurement of the area of the bond, or [52], in which a platform has been developed in charge of creating, manipulating and breaking individual paper fiber bonds in order to measure the strength of the bond. A better understanding of paper fiber bonds can lead to the decrease of rips that commonly take place in paper mills and to the enhancement of the properties of paper.

One of the steps in the manufacture of paper fiber bonds consists of pressing paper fibers together with a careful control on the pressure exerted. This task can be easily

handled by means of a piezoelectric stack and a force control scheme designed for it. Piezoelectric actuators have found their way in a variety of applications, and pose a great interest in micromanipulation thanks to the generation of precise movements and high forces even in the nanometer range and the high reaction speeds [21].

1.2. Objective of the Thesis

The purpose of the piezoelectric stack being the creation of paper fiber bonds and the execution of compression tests means that force control needs to be applied to the actuator in order to achieve an adequate performance.

Closed-loop force control methods for piezoelectric actuators have been remarkably researched and different configurations have been tested to deal with some of the issues derived from working in the micro scale, such as the one for increased sensitivity proposed in [11] or the one for multiple degree sensing mentioned in [61]. At first glance, a feedback control technique might be considered because of its robustness, among other reasons, but the sizes of accurate force sensors make them difficult or even impossible to implement in certain applications.

A possible alternative to the use of force sensors lies on force estimation. Force estimation has been successfully implemented thanks to the self-sensing capabilities of the piezoelectric actuators [5] or the possibility to estimate the force from other parameters of the system [40].

Another alternative to the use of force sensors can be found in open-loop or feedforward control techniques. While not robust against changes of the parameters of the system or changes in the environment, open-loop control poses an interesting and simple to implement option and enhances miniaturization thanks to the lack of sensors of any kind. Nevertheless, this approach has not been thoroughly researched and barely a few publications have dealt with it.

Thus, the objective of this thesis consists of designing an open-loop control scheme and implementing it to the piezoelectric stack, verify the results and confirm the possibility to use such control techniques for micromanipulation with a piezoelectric actuator. The control method will be particularly based on previous research on open-loop compensation techniques for displacement in piezoelectric actuators such as [42] or [54].

1.3. Organization of the Thesis

The thesis has been divided into different chapters as follows: Chapter 2 provides the necessary theoretical background to better understand the topic and the methods later described; Chapter 3 includes a description of the control methods proposed, as well as a list of the software and hardware required for the tests; processing of the signal coming from the sensor will be dealt with in Chapter 4 before tackling the characterization of the actuator, which will be faced in Chapter 5; Chapter 6 will

describe the implementation and verification of the control schemes; finally, Chapter 7 will conclude the thesis by summarizing and discussing the results as well as proposing the subject of further research on the topic at hand.

2. Theoretical Background

In piezoelectric materials an electrical charge appears on the surfaces when mechanical stress is applied to them. This effect finds its main use in sensoring applications, where piezoelectric materials are implemented in acoustic sensors, pressure/force sensors and even accelerometers. However, it is not piezoelectricity but the inverse effect, the transduction of electrical energy into mechanical energy, that offers a variety of possibilities in actuating applications. Motors, grippers, sound generators and fluid dispensers are some of the most common uses for piezoelectric actuators.

As with any other kind of actuation technology, piezoelectric actuators might require the implementation of a controller for an acceptable performance. Displacement control is essential in positioning applications and many techniques have been thoroughly researched and implemented successfully. Force control is oriented mainly to force testing applications and to prevent elements from being damaged in manipulation processes, and in relation to displacement control not many techniques have been studied and developed to this day.

This chapter provides the theoretical background needed for the topic. The piezoelectric effect and its inverse are studied in Section 2.1. Section 2.2 offers some insight on the most common types of piezoelectric actuators and their working principles. Last, Section 2.3 introduces force control for piezoelectric actuators and gathers some of the most recent and relevant force control techniques.

2.1. Piezoelectricity

The piezoelectric effect was discovered in 1880 by Pierre and Jacques Curie after conducting several tests on a variety of crystals, such as tourmaline, quartz or cane sugar, and observing that positive and negative charges appeared on their surfaces after they had been mechanically stressed in different directions [47]. It was not until a year later that Hankel proposed the term *piezoelectricity*, referring to "electricity by pressure" (*piezo* or *piezein* are Greek words which mean squeeze or press), to name the phenomenon discovered by the Curie brothers [4]. Shortly after, Lippmann predicted the converse effect through the fundamental principles of thermodynamics and the Curies confirmed its existence following his work [47].

Thus, the direct piezoelectric effect is understood the generation of an electric charge in a material as a result of a force applied to it, while the inverse piezoelectric effect means the deformation of the material when a certain voltage is applied to it. It can be inferred from this that the technologies that benefit from the direct piezoelectric effect are mainly those with sensing [18], [23], [55], [64] and power harvesting [39],

[51] applications. On the other hand, piezoelectric actuators base their working principle on the inverse piezoelectric effect [24].

The piezoelectric effect can also be seen as the modification of the polarization of a dielectric in response to an applied mechanical stress. In order for the piezoelectric effect to take place it is required that the material is anisotropic, that is, that there is a dominant direction for polarization [38]. Therefore, in the case of isotropic materials (such as ferroelectric or ferromagnetic) they need to be subjected to a poling process consisting on heating the material above the Curie temperature (point at which a ferromagnetic material becomes paramagnetic), then cooling it down while an external electric field is applied that imposes the orientation of the polarization. Without this poling process the electric dipoles of each individual crystal comprising the material are cancelled with the neighboring electric dipoles and the piezoelectric properties are non-existent.

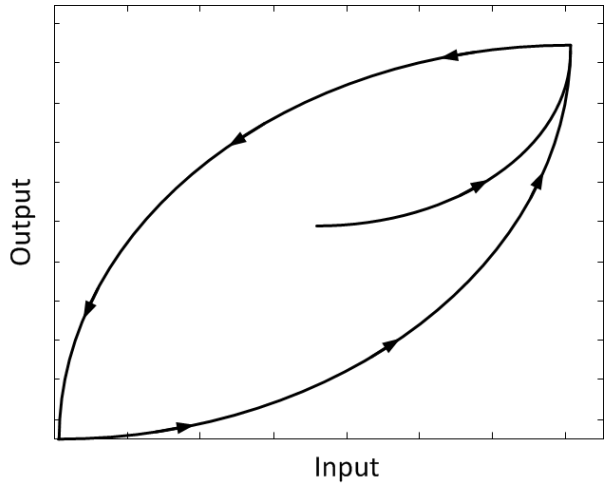

Figure 2.1. *Representation of the hysteresis phenomenon, present in piezoelectric materials.*

When operating piezoelectric materials under low input magnitudes (either electric field or mechanical stress) the transduction can be considered to be completely linear. However, when higher drives are used the linear behavior disappears and gives way to a hysteretic non-linearity. Hysteresis is commonly considered to be caused by the residual misalignment of several regions with different dipole directions after the poling process [32], [47]. When subjecting the material to an increasing electric field the regions with unfavorable dipole direction start to switch to the closest possible direction parallel to the direction of the applied electric field. If, once reached a specific point, the electric field applied starts to decrease the required field to switch these regions back to a previous position is smaller, thereby proving the non-linear relation between the electric field applied and the displacement/force obtained. The hysteresis phenomenon is depicted in Figure 2.1. Also, hysteresis in piezoelectric materials is not only dependent on the amplitude of the electric field applied, but also on its frequency [47], [63]. This is why it is said to be a dynamic or rate-dependent hysteresis.

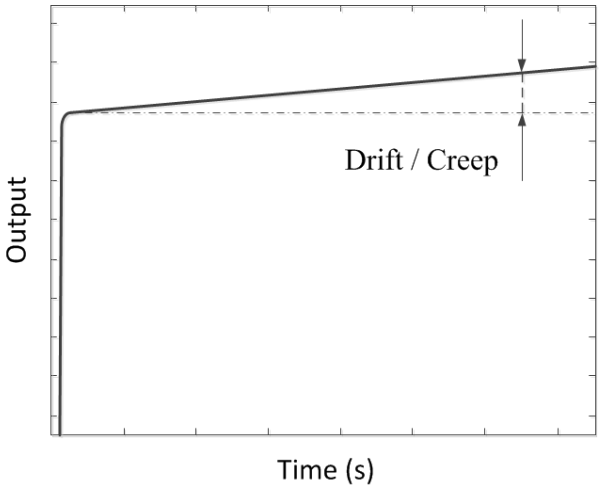

Figure 2.2. *Representation of the drift or creep phenomenon, present in piezoelectric materials.*

Another phenomenon present in piezoelectric materials is creep. Creep can be described as the slow drift in the displacement of a piezoelectric material as a result of the applied electric field over a long period of time [31], as depicted in Figure 2.2. Even with small fields, their action taking place during an extended time forces the misaligned regions to keep on correcting their deviation with respect to the direction of the applied electric field, resulting in a continuously growing displacement.

2.2. Piezoelectric Actuators

Piezoelectric actuators include a great variety of transducers that can be divided into two big groups depending on their operation principle: resonant and non-resonant piezoelectric actuators [38].

The key parameter in resonant piezoelectric actuators is the frequency of the excitation. When turning that frequency to the resonance or antiresonance frequency, a microscopic resonant vibration will take place inside of the material that can be transformed into a macroscopic linear or rotary motion. Thus, resonant piezoelectric actuators are commonly referred to as ultrasonic motors. However, resonant piezoelectric actuators not only include linear [28] and rotatory [14] ultrasonic motors, but also open up the possibility of travelling wave ultrasonic motors [13].

On the other hand, driving of non-resonant piezoelectric actuators relies on the amplitude of the excitation voltage. The characteristics of non-resonant piezoelectric actuators make them generally ideal for precision positioning devices, although some configurations have proven to be also useful in the manipulation of objects, as force applying devices, etc.

Piezoelectric stack actuators include a large number of thin piezoelectric plates placed one on top of each other with common electrodes situated between consecutive layers, causing a mechanical displacement in one of the ends of the structure when a

driving voltage is applied. The driving voltages, as well as the displacements observed, are typically small, but considerably high forces are achieved. Also, in piezostacks the strain and stress relation can be considered to be linear, obeying Hook's law. They can be used in a variety of applications, such as liquid dispensers [33], [65] or positioning devices [10].

Piezoelectric bimorphs consist of two thin piezoelectric plates with a specific relative polarization that causes the simultaneous expansion of one of the plates and the contraction of the other when the driving voltage is applied, achieving relatively high deflections of the whole structure and small forces. They are typically used as manipulation devices in piezoelectric grippers [1], [16].

Certain configurations of non-resonant piezoelectric actuators can also be used as motors, and therefore overcome the small motion range that characterizes the previously mentioned actuators. Such is the case of inchworm motors [67] or stick-slip drivers [48].

2.3. Force Control for Piezoelectric Actuators

Ever since piezoelectric materials started being considered for actuation applications in the field of microsystems much has been researched and written on displacement control. However, while the control of the displacement is essential in applications related to positioning, when using the actuator for manipulation purposes force control will also be required in order to ensure proper contact between the actuator and the manipulated object or simply to prevent the manipulated object from being damaged or even destroyed.

Contrary to what happens with displacement control methods, to this day not many control techniques have been developed for force control. The most common approach is based on gathering knowledge on the target object, in order to use the information collected and compare it to a reference, a task that can be faced following different possible methods.

Closed-loop control, possibly the most obvious and classical technique, involves the use of force sensors, typically strain gages or load cells. The main problem with this approach in microsystems is the necessity of a force sensor capable of sensing in the micro scale, in some cases with resolutions in the order of nN and/or with multiple sensing degrees of freedom. The most precise conventional strain gages or load cells show a resolution in the order of μN, so either specially designed force sensors or special configurations have to be considered to achieve the desired characteristics. Such is the case of the sensor used in [61], comprising two strain gages of semiconductor resistor, each of them with an opposite gage factor in order to obtain a high output signal even with small displacements of a cantilever.

Some configurations also aim to deal with other problems derived from measuring in the micro scale, such as the increased sensitivity against changes in the environment and the levels of noise being more critical than in the macro scale. One example is the

configuration proposed in [11] for the sensors for a microgripper, consisting of a full Wheatstone bridge based on four active strain gauges.

As mentioned before, multiple sensing degrees are possible by using several sensors or some specific configurations. In [61], sensing in two directions with microgrippers is proved to be possible by using two sensors instead of one and therefore increasing the success rate of the grasping operation.

However, it will not be always possible to implement and use force sensors in the systems designed. Force sensors are typically bulky and costly, making them unsuitable for certain applications. Nevertheless, the impossibility of using force sensors should not be seen only as a source of complexity for the problem at hand, but as a possibility to simplify the mechanism and enable further miniaturization. Alternative techniques rely on force estimation from one or several other parameters measured from the system being controlled. A force estimator is but a linear or nonlinear model that helps approximate the external force. Force estimation offers an ample range of possibilities, but is can also prove to have its own inherent difficulties.

Given the reciprocity of the piezoelectric effect, it is quite common in force estimation to make use of the self-sensing capabilities of the materials, that is, to make use of the material as both sensor and actuator. A force estimation model based on the input voltage and the current measured from the actuator is proposed in [5]. Self-sensing is not easy and can be hindered by changes in environmental conditions. A study on the effect of such changes and possible solutions to this problem are presented in [56]. Self-sensing possibly offers the best chances for further miniaturization due to the absence of additional devices and is generally destined to vibration control and suppression, but it has also been found to be useful in other actuation applications. However, there are two critical issues related to self-sensing that still need to be perfected: a very good precision is required when measuring the electrical charge, and perturbations in the voltage can be the cause of considerable discrepancies, and might need to be seriously considered depending on the application requirements.

Other options entail measuring another parameter or parameters and estimating the force from them. Such is the case of the estimator developed in [40], using the information provided by a laser sensor on the displacement of a cantilever. Laser sensors are also bulky and expensive, but do not need to be placed right next or in direct contact with the actuator.

More complex models have been studied and tested. A model where force is estimated by using self-sensing aided with the information provided by a laser sensor, that is, from the input voltage, the current measured from the actuator and the displacement measured, can be found in [44], [49] and [50]. This solution proved however to be quite inaccurate with high loads, but could be adequate for certain robotic tasks.

Control in closed-loop can be simply managed by the implementation a PI or PID controller. PI controllers have been successfully used in [11] for a microgripper, to

ensure the contact with the object and that not too much force is applied during the pick-up task, and in [49] for a piezocantilever, while in [5] the control of a piezostack is dealt with by means of a PID controller.

While PI or PID controllers might be the easiest solution, in force control this might not be the most adequate of all the possible solutions. When developing a model for the actuator it becomes obvious that said model will depend on the characteristics of the manipulated objects. Due to the wide range of applications for piezoelectric actuators, the manipulated items will exhibit very different characteristics (shape, stiffness, elasticity, etc.) and a general method for control cannot be established. Failing to acknowledge this can lead to control schemes being rendered completely useless if, for example, the object does not have a specific shape or surface finishing. Of course, precise modeling of an actuator that takes into consideration the characteristics of the objects to manipulate is not an easy task, and in some cases a better solution needs to be sought.

Not being practical to identify the whole model and synthesize a controller for every different type of sample, a possible solution is to use a robust controller that ensures the stability and a good performance even with uncertain parameters or in the presence of disturbances. The performance of a microgripper is controlled in [40] by means of two H_∞ robust controllers: one is in charge of the displacement control of one of the fingers while the other deals with the force control of the other finger. Instead of modeling the whole system, the behavior of each finger is modeled separately. This way, the effect of one finger on the other is considered a disturbance that can be taken care of thanks to the robust control. Therefore, robust control can be used to simplify the overall design.

Despite the fact that robust controllers can adapt to many different situations, any of the characteristics of the objects manipulated could vary in such a wide range of possible values that the aforementioned solution might not be enough and stability could not be guaranteed. It is however possible to develop a parameter-dependent approach that could ensure a specified performance with different manipulated objects. A self-scheduled controller dependent on one of the parameters of the manipulated elements is proposed in [46], and proved to be able to adapt to several different cases.

Another alternative to force control that does not require force sensors and therefore enhances miniaturization is open-loop force control. This is, however, an approach that has not been thoroughly studied and has been discussed in merely a few publications so far. The open-loop displacement control designed in [42] for hysteresis, drift and vibration compensation is mentioned to be also apt for force control. On the other hand, a full open-loop force control for stick-and-slip drives is proposed in [9].

3. Methods and Materials

This chapter introduces the control methods to be implemented in the experiments carried out in this thesis, as well as the software and hardware necessary for said experiments.

This chapter has been divided into three differentiated sections. Section 3.1 presents the open-loop control method proposed in its three subsections, which deal with the hysteresis, creep and vibration compensation. Finally, Section 3.2 and Section 3.3 describe the required software and hardware respectively.

3.1. Control Method

The control scheme proposed for this thesis work consists of an open-loop compensation of the nonlinearities of the system, i.e. hysteresis and drift or creep, and undesired vibrations. Open-loop control is based on providing an input to a system computed from only the current state and a model of the system, and therefore eliminating the necessity found in feedback control to measure the output by means of a sensor or a similar device. Since the system will not be able to observe the output of the process the controlling errors cannot be corrected and the disturbances or the effect of unexpected parameter variations cannot be rejected. However, and as it was already mentioned in the previous chapter, open-loop control techniques are of great interest in micromanipulation due to the versatility stemming from the absence of a force sensor, typically bulky and expensive.

The control will be divided into three different blocks, each in charge of the compensation of one of the aforementioned parameters. The order in which each of the compensations is applied to the signal can be observed in Figure 3.1. All the techniques used here have been successfully tested and implemented in displacement control of piezoelectric actuators, and will be adapted if necessary in order to extend them to force control.

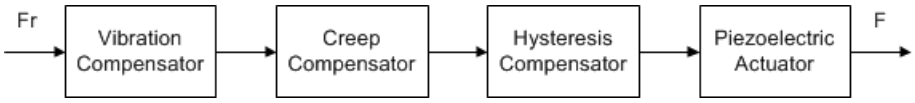

Figure 3.1. *Block diagram of the open-loop compensation to be used in this thesis work.*

The design of these blocks will be discussed in the next subsections in the following order: first, the hysteresis will be compensated based on an identified model in Section 3.1.1; then, the creep of the improved system will be modeled and a compensation technique based on an inverse multiplicative structure will be applied to it in Section

3.1.2; last, Section 3.1.3 presents an input shaping method to rid the system of vibrations.

3.1.1. Hysteresis Compensation

In the introduction chapter, it was explained that hysteresis in piezoelectric actuators is commonly dynamic or rate-dependent, meaning that it varies with frequency. More specifically, hysteresis tends to increase when frequency or rate is increased.

One common way to approach open-loop hysteresis compensation consists of modeling said hysteresis and subsequently developing an inverse model from it which can be implemented in series with the real system, as illustrated in Figure 3.2. Thus, the input of the system will be a reference signal that the output should follow as closely as possible.

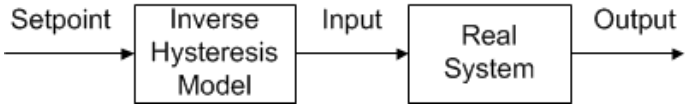

Figure 3.2. *Open-loop control for the hysteresis by means of an inverse hysteresis model.*

A number of mathematical models for hysteresis have been proposed over the years. The Preisach model has been successfully applied for modeling static hysteresis, although the method can also be generalized for dynamic hysteresis [20], [53]. The Bouc-Wen model is another option for modeling static hysteresis [43]. A variation of the Preisach model is the Prandtl-Ishlinskii model, or PI model for short, is commonly used for modeling static hysteresis [27], [41], [42], although a modified approach makes it possible to use for modeling rate-dependent hysteresis [3].

In addition, it has been proven that in piezoelectric actuators dynamic hysteresis can be modeled as static hysteresis in series with a linear dynamic part [41], [45], as shown in Figure 3.3.

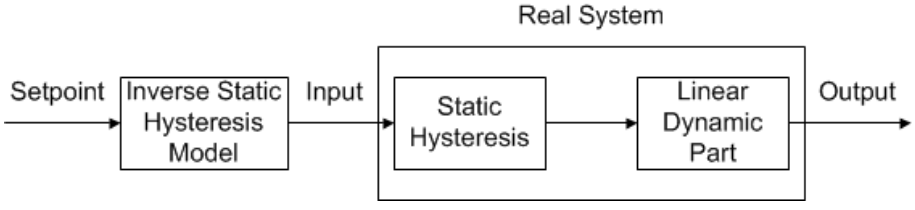

Figure 3.3. *Diagram depicting the division of the hysteresis of the real system into static hysteresis and a linear dynamic part.*

The PI model for static hysteresis offers bigger simplicity of implementation, is more attractive for real-time applications and its inverse model can be computed analytically, making it more adequate than others for the task at hand. Thus, and relying on the possibility to separate hysteresis into static hysteresis and a transient part, the compensation technique proposed for this thesis will only deal with static hysteresis

since the application for which the piezoelectric stack to be controlled is destined does not require working at high frequencies.

Originally the PI model is only applicable when the hysteresis is symmetrical and non-saturated, and thereby limiting considerably its practical use. If the hysteresis to model was non-symmetrical and/or saturated the original PI model is no longer of use and a different approach needs to be taken. A modified Prandtl-Ishlinskii operator has been proposed by different authors in such a case [3], [25], [54], [59]. This variation of the PI model relies on the use of two different operators, each with a different function.

The first operator is known as backlash operator, and provides symmetry to the hysteresis. A backlash operator makes the output of the system change equally to the input, except when the input changes direction, having no effect on the output as long as it is inside a range of values centered about the output known as deadband, limited by a threshold value *r*. The principle of a backlash operator is illustrated in Figure 3.4 for a better understanding.

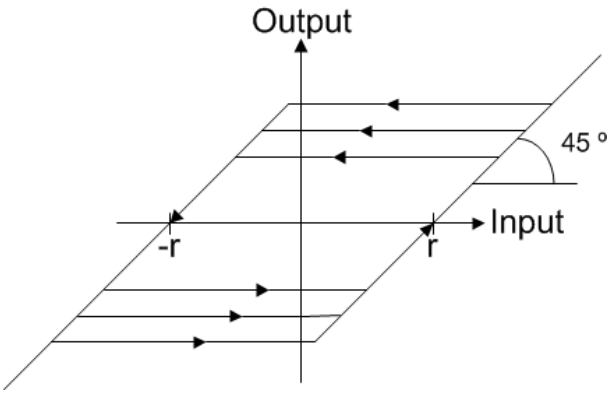

Figure 3.4. *Representation of the function realized by the backlash operator.*

The mathematical expression that describes the backlash operator is the following one:

$$y(t) = H_r[x, y_0](t) = \max\{x(t) - r, \min\{x(t) + r, y(t - T_s)\}\} \quad (3.1)$$

Where x is the input, y is the output, r is the control input threshold value or deadband of the backlash and T_s is the sampling period.

An initial condition is also needed as is normally expressed as:

$$y(0) = \max\{x(0) - r, \min\{x(0) + r, y_0\}\} \quad (3.2)$$

Where y_0 is the initial state and is usually initialized to 0, considering that the system starts from a de-energized state.

Introducing a weighing coefficient w that establishes the output to input ratio or gain of the operator we will obtain the generalized expression for the backlash operator, which is:

$$y(t) = w_h H_r[x, y_0](t) \tag{3.3}$$

When the model becomes more and more complex, the necessity of using several backlash operators might arise. In such a case, the expression has to be modified to indicate the superposition of the n different operators, each of them with their own weighing coefficient w_{hi} and initial state y_{0i}:

$$y(t) = \sum_{i=0}^{n} w_{hi} H_{r_i}[x(kT_s), y_{0i}] \tag{3.4}$$

As mentioned previously, if the system is considered to start from a de-energized state then:

$$y_{0i} = 0, \qquad \forall i \tag{3.5}$$

In order to account for the lack of symmetry a second operator is included in addition to the backlash operator: the one-sided dead zone operator. The one-sided dead zone operator generates zero output within a specified region known as the dead zone d, and makes the output of the system change equally to the input outside of said zone, as depicted in Figure 3.5.

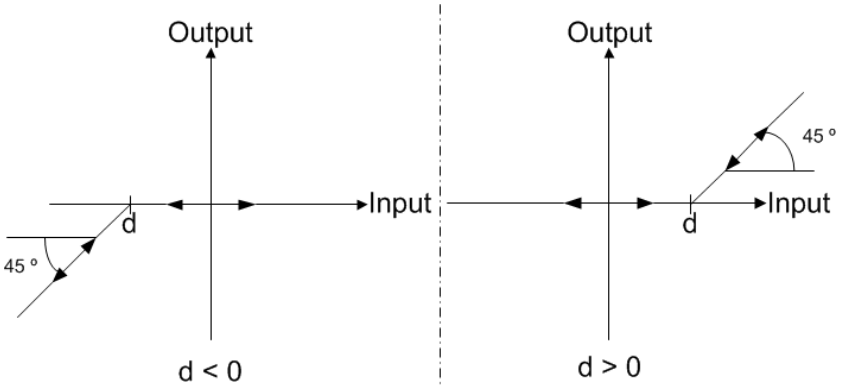

Figure 3.5. *Representation of the function realized by the one-sided dead zone operator.*

The operator is defined by the following expression:

$$z(t) = S_d[y] = \begin{cases} \max\{y - d, 0\}, & d > 0 \\ y, & d = 0 \\ \min\{y - d, 0\}, & d < 0 \end{cases} \tag{3.6}$$

Where y is the input, z the output and d is the control input threshold value or dead zone of the one-sided dead zone operator.

When dealing with complex models and with the inclusion of weighing coefficients w_{sj} to establish the output to input ratio, the superposition of m one-sided dead zone operators can be expressed in a similar way to Equation (3.4):

$$z(t) = \sum_{j=-m}^{m} w_{sj} S_{d_j}[y] \tag{3.7}$$

Thanks to these two operators hysteresis can be modeled by a linearly weighted superposition of backlash operators with different deadbands and weights in series with a linearly weighted superposition of one-sided dead zone operators with different dead zones and weights as illustrated in Figure 3.6 and seen in the following formula:

$$z(t) = H[x(kT_s)] = \sum_{j=-m}^{m} w_{sj} S_{d_j}\left[\sum_{i=0}^{n} w_{hi} H_{r_i}[x(kT_s), y_{0i}]\right], \qquad k = 1..n_s \tag{3.8}$$

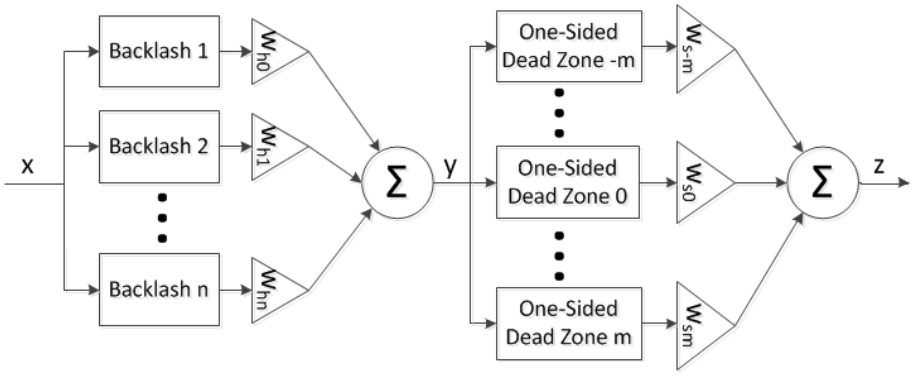

Figure 3.6. *Block diagram of the PI hysteresis model.*

Where w_{hi} and w_{sj} are the weights of the backlash and dead zone operators respectively, r_i are the control input threshold values or magnitudes of the backlashes sorted so that $0 = r_0 < r_1 < \cdots < r_n$, d_j are the control input threshold values sorted so that $d_{-m} < \cdots < d_{-1} < d_0 = 0 < d_1 < \cdots < d_m$, y_{0i} are the initial states and n_s is the quantity of sampled data.

As a common rule, the values of r_i and d_j are chosen to be equally spaced in the admissible range of values. However, observations have suggested that the most drastic changes occur in the region of the first few backlashes operators [58], implying that special attention should be paid on said region and that backlash operators beyond the midpoint of the control input range rarely contribute to the model at all and can even be sometimes omitted. This might lead to using finer intervals on the initial values for better accuracy on the model.

In an analogous manner, the inverse model will be given by Equation (3.9) and has been depicted in Figure 3.7.

$$x(t) = H^{-1}[y(kT_s)] = \sum_{i=0}^{n} w'_{hi} H_{r'_i} \cdot \left[\sum_{j=-m}^{m} w'_{sj} S_{d'_j}[y(kT_s)], z_{0i} \right], \qquad k = 1..n_s \quad (3.9)$$

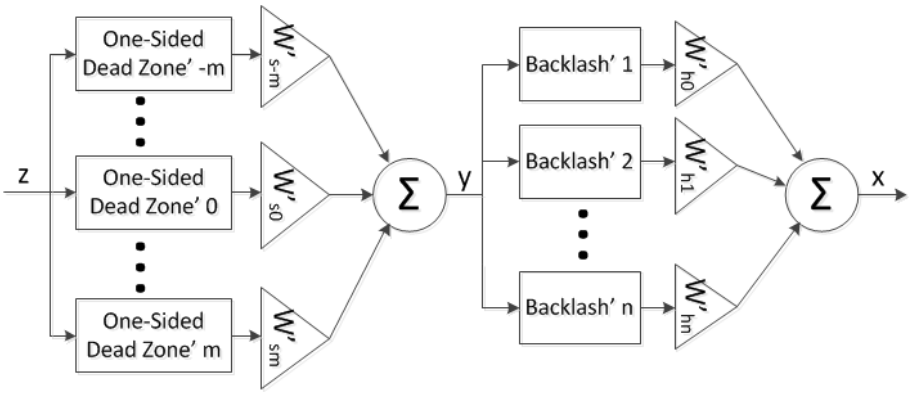

Figure 3.7. *Block diagram of the inverse PI hysteresis model.*

Where w'_{hi} and w'_{sj} are the weights of the backlash and dead zone operators respectively, r'_i are the control input threshold values or magnitudes of the backlashes sorted so that $0 = r'_0 < r'_1 < \cdots < r'_n$, d_j are the control input threshold values sorted so that $d'_{-m} < \cdots < d'_{-1} < d'_0 = 0 < d'_1 < \cdots < d'_m$, z_{0i} are the initial states and n_s is the quantity of sampled data.

It is important to know that this inverse model can be found only as long as the weights of the backlash and one-sided dead zone operators of the direct hysteresis model are non-negative [58], [60]. If any of the weights was negative, it would mean that the largest output would not take place at the maximum input signal and a singularity would occur in the inverse. It is however possible to find a singularity-free variant of the PI model [60], although this will not be covered in this thesis work.

Typically, the computation of the parameters of the direct and inverse hysteresis models starts with an optimized fit of (3.8) to the experimentally measured hysteresis, searching to minimize the following error Equation:

$$E[x, z] = \sum_{i=0}^{n} w_{hi} H_{r_i}[x(kT_s), y_{0i}] - \sum_{j=-m}^{m} w'_{sj} S_{d'_j}[z(kT_s)] \quad (3.10)$$

Some authors propose that the direct and inverse PI hysteresis models can be more easily calculated by simply using information extracted from the initial loading curve of the hysteresis [58]. This method will however not be applied since the least-square optimization of Equation (3.10) will allow us to use the complete measured hysteresis curve and thereby will provide better accuracy.

In [54] a quadratic optimization is proposed for the error, through which the weight parameters w_{hi} and w'_{sj} will be obtained. The expression to be optimized is:

$$\min_{w}\{w^T \Omega^T \Omega w\} \tag{3.11}$$

Where:

$$w^T = [w_{h0} \quad \dots \quad w_{hn} \quad w'_{s(-m)} \quad \dots \quad w'_{s0} \quad \dots \quad w'_{sm}] \tag{3.12}$$

$$\Omega = [\Omega_H \quad \Omega_S] \tag{3.13}$$

$$\Omega_H = \begin{bmatrix} H_{r_0}[x(0), y_{00}] & \cdots & H_{r_n}[x(0), y_{0n}] \\ H_{r_0}[x(T_s), y_{00}] & \dots & H_{r_n}[x(T_s), y_{0n}] \\ \vdots & \ddots & \vdots \\ H_{r_0}[x(n_s T_s), y_{00}] & \cdots & H_{r_n}[x(n_s T_s), y_{0n}] \end{bmatrix} \tag{3.14}$$

$$\Omega_S = \begin{bmatrix} -S_{d'_{-m}}[y(0)] & \cdots & -S_{d'_0}[y(0)] & \cdots & -S_{d'_m}[y(0)] \\ -S_{d'_{-m}}[y(T_s)] & \dots & -S_{d'_0}[y(T_s)] & \cdots & -S_{d'_m}[y(T_s)] \\ \vdots & \ddots & \vdots & \ddots & \vdots \\ -S_{d'_{-m}}[y(n_s T_s)] & \cdots & -S_{d'_0}[y(n_s T_s)] & \cdots & -S_{d'_m}[y(n_s T_s)] \end{bmatrix} \tag{3.15}$$

With the constraints:

$$\begin{bmatrix} U_H & 0 \\ 0 & U_S \end{bmatrix} w - \begin{bmatrix} u_H \\ u_S \end{bmatrix} \leq \begin{bmatrix} 0 \\ 0 \end{bmatrix} \tag{3.16}$$

$$[(\|x\|_\infty I - r)^T \quad 0^T] w - \|x\|_\infty = 0 \tag{3.17}$$

Where:

$$U_H = \begin{bmatrix} -1 & 0 & \cdots & 0 \\ 0 & -1 & \cdots & 0 \\ \vdots & \vdots & \ddots & \vdots \\ 0 & 0 & \cdots & -1 \end{bmatrix} \tag{3.18}$$

$$U_S = \begin{bmatrix} -1 & \cdots & -1 & -1 & 0 & \cdots & 0 \\ \vdots & \ddots & \vdots & \vdots & \vdots & \ddots & \vdots \\ 0 & \cdots & -1 & -1 & 0 & \cdots & 0 \\ 0 & \cdots & 0 & -1 & 0 & \cdots & 0 \\ 0 & \cdots & 0 & -1 & -1 & \cdots & 0 \\ \vdots & \ddots & \vdots & \vdots & \vdots & \ddots & \vdots \\ 0 & \cdots & 0 & -1 & -1 & \cdots & -1 \end{bmatrix} \tag{3.19}$$

$$u_H^T = [-\varepsilon \quad 0 \quad \cdots \quad 0] \tag{3.20}$$

$$u_S^T = [-\varepsilon \quad -\varepsilon \quad \cdots \quad -\varepsilon] \tag{3.21}$$

$$I^T = [1 \quad 1 \quad \cdots \quad 1] \tag{3.22}$$

$$r^T = [r_0 \quad r_1 \quad \cdots \quad r_n] \tag{3.23}$$

And ε is a small positive number. At this point it is convenient to remember that if the system is considered to start from a de-energized state then:

$$y_{0i} = 0, \qquad \forall i \tag{3.24}$$

The values of r_i and d'_j are determined using experimental data as follows:

$$r_i = \frac{i}{n+1} \max_k\{|x(kT_s)|\}, \quad i = 1 \,..\, n \tag{3.25}$$

$$d'_j = \frac{(j - 1/2)}{m} \max_k\{y(kT_s)\}, \quad j = 1 \,..\, m \tag{3.26}$$

$$d'_j = \frac{(-j - 1/2)}{m} \min_k\{y(kT_s)\}, \quad j = -m \,..\, -1 \tag{3.27}$$

After the optimization and once the weight parameters w_{hi} and w'_{sj} have been found, the rest of the parameters of both the direct and the inverse model can be calculated as shown in Equation (3.28) to Equation (3.36).

$$w'_{h0} = \frac{1}{w_{h0}} \tag{3.28}$$

$$w'_{hi} = \frac{-w_{hi}}{\left(\sum_{l=0}^{i} w_{hl}\right)\left(\sum_{l=0}^{i-1} w_{hl}\right)}, \qquad i = 1 \,..\, n \tag{3.29}$$

$$r'_i = \sum_{l=0}^{i} w_{hl}(r_i - r_l), \qquad i = 0 \,..\, n \tag{3.30}$$

$$w_{s0} = \frac{1}{w'_{s0}} \tag{3.31}$$

$$w_{sj} = \frac{-w'_{sj}}{\left(\sum_{l=1}^{j} w'_{sl}\right)\left(\sum_{l=1}^{j-1} w'_{sl}\right)}, \qquad j = 1 \,..\, m \tag{3.32}$$

$$w_{sj} = \frac{-w'_{sj}}{\left(\sum_{l=j}^{0} w'_{sl}\right)\left(\sum_{l=j+1}^{0} w'_{sl}\right)}, \qquad j = -m \,..\, -1 \tag{3.33}$$

$$d_0 = 0 \tag{3.34}$$

$$d_j = \sum_{l=0}^{j} w_{sl}\left(d_j - d_l\right), \qquad j = 1 \,..\, m \tag{3.35}$$

$$d_j = \sum_{l=j}^{0} w_{sl}\left(d_j - d_l\right), \qquad j = -m \,..\, -1 \tag{3.36}$$

The number n of backlash operators and m of one-sided dead zone operators to be used should be defined by trial and error, starting from a small and reasonable order and increasing it until the identified model is considered to be similar enough to the experimental result. It should be kept in mind that a bigger quantity of these operators leads to a better accuracy, but a smaller number makes them easier to calculate and implement.

3.1.2. Creep Compensation

Inverse modeling is probably the most common way to deal with open-loop creep compensation [19], but other approaches do not require direct model inversion and can prove to be more practical and easier to implement.

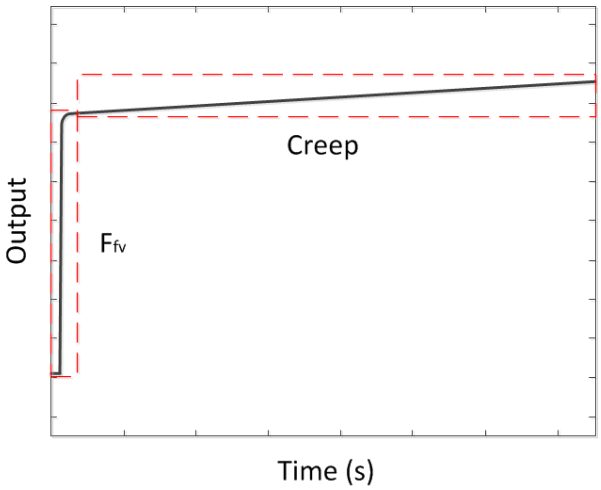

Figure 3.8. *Division of the creeped response into a constant signal F_{fv} and the creep.*

Such is the case of the method proposed in [42]. Starting from the hysteresis compensated system, creep can be identified and modeled. Since creep is a phenomenon

that takes place mostly at low frequencies an input signal with those characteristics should be used. Thereby, creep will be easily observed if a step input signal is used during a prolonged period of time.

Taking into consideration that hysteresis compensation was tackled by means of an inverse model, the current response of the system should follow the input signal with relative accuracy. However, if the system suffers from creep this will not be the case and the response will drift away from the value of the input signal.

Ignoring the transient part (that will be approached in the next section) this response can be considered as the sum of a constant signal with the value F_{fv} and another signal depicting the drift, as shown in Figure 3.8. Naming the linear static gain F_{fv}/F_h, where F_h is the hysteretic reference input, as K_c (note that this value might or might not be 1, depending on the accuracy of the linearization achieved with the hysteresis compensation) and the transfer function of the creep model as *C(s)*, a model for the hysteresis compensated system can be expressed as:

$$\frac{F}{F_h} = \left(K_c + C(s)\right) \tag{3.37}$$

Both the creep *C(s)* and the static gain K_c (in case its value differs from 1) can be easily compensated using an inverse multiplicative scheme, as shown in Figure 3.9.

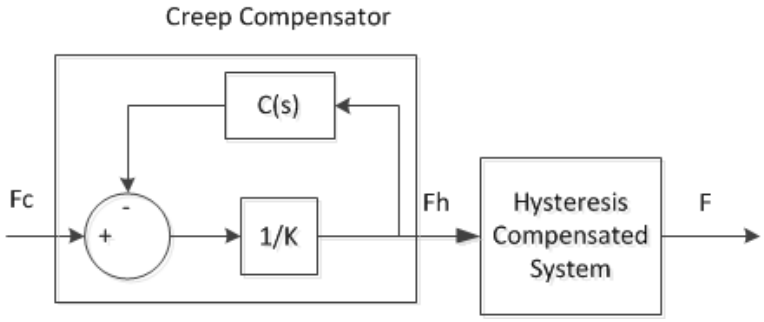

Figure 3.9. *Inverse multiplicative structure for creep compensation.*

Where F_c is the hysteretic, creeped force reference input. Thus, the transfer function of the creep compensator will be as follows:

$$\frac{F_h}{F_c} = \frac{1}{\left(K_c + C(s)\right)} \tag{3.38}$$

And of course, the transfer function of the whole compensated system will be:

$$\frac{F}{F_c} = \frac{F}{F_h}\frac{F_h}{F_c} = \frac{1}{\left(K_c + C(s)\right)}\left(K_c + C(s)\right) = 1 \tag{3.39}$$

Which means that the creep or drift of the system should be theoretically completely compensated thanks to this technique.

3.1.3. Vibration Compensation

So far, the compensations of the low frequency nonlinearities have been taken care of: static hysteresis and creep. Now, all that is left is treating the fast dynamic characteristics.

To observe these characteristics we need to obtain the step response of the system with the compensations applied so far. If the system is badly damped, as the one depicted in Figure 3.10, high overshoots and prolonged oscillations may occur. These features affect seriously the performance of the actuator, causing high forces to be applied before reaching the desired value.

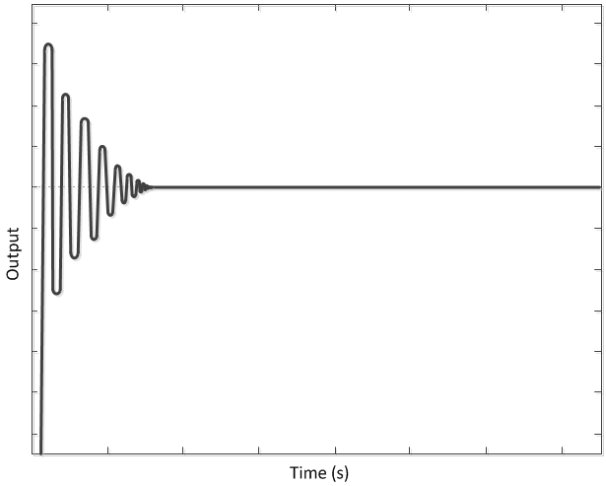

Figure 3.10. *Badly damped system, with high overshoot and oscillations.*

One possible solution for this problem is input shaping. Input shaping has been commonly used in computer-controlled machines reducing residual vibrations of oscillating systems, thereby decreasing the overshoot and improving settling time and positioning accuracy. Implementation consists of dividing the input signal into a sequence of impulses, which are convoluted to produce a desired shaped input. Out of the different techniques available for input shaping the most interesting and commonly used in oscillating systems are the Zero-Vibration (or ZV) input shaping technique [6], [15] and its variants (such as the Zero-Vibration-Derivative [12] or the Zero-Vibration-Derivative-Derivative [2]), although other techniques are also available [57].

In particular, the ZV input shaping method has been successfully used for the elimination of vibrations in the displacement of a piezoelectric microgripper in [42], and therefore posing a bigger interest with respect to the objective of this thesis work. The principle followed by the ZV input shaping technique is the following: considering that applying an impulse to the oscillating system will result in vibrations, if the input signal is divided into different impulses with carefully selected amplitudes and delays with respect to each other, the vibration caused by every impulse can cancel or be cancelled by those of the other impulses. Figure 3.11 illustrates this compensation principle when using two impulses.

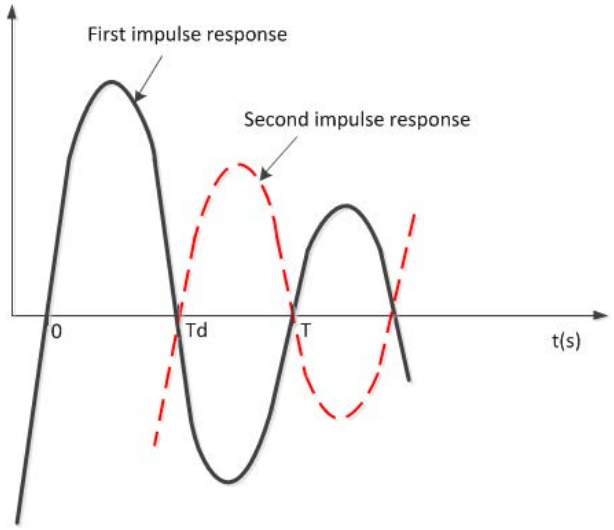

Figure 3.11. *Compensation principle of the ZV input shaping technique with two impulses.*

The delay for each impulse needs to be half of the period T of the original signal. This period T can be measured directly from the signal, or calculated from the natural frequency w_n and damping ratio ξ if the vibrations are modeled and identified as the step response of a second order system as follows:

$$T = 2\pi/w_n\sqrt{1-\xi^2} \tag{3.40}$$

And the aforementioned model will have the following transfer function:

$$\frac{F}{F_c} = \frac{K_v}{(\frac{1}{w_n})^2 s^2 + \frac{2\xi}{w_n}s + 1} \tag{3.41}$$

Where F is the force output, F_c is the hysteretic and creeped force, K_v is the static gain of the system after applying the creep and hysteresis compensations.

The computation of the amplitudes of the impulses proposed in [42] and [6] is based on these identified parameters. Thus, the time domain expression for the vibrations caused by each impulse F_i is:

$$F_i(t) = \frac{K_v A_i w_n}{\sqrt{1-\xi^2}} e^{-[(t-t_i)\xi w_n]} \sin(w_n(t-t_i)\sqrt{1-\xi^2}) \tag{3.42}$$

Where A_i is the amplitude and t_i the delays applied to each impulse.

As the name of the technique implies, the objective is to have an output with no vibrations, and therefore:

$$\sum_{i=1}^{p} F_i(t) = 0 \tag{3.43}$$

Where p is the number of impulses used.

The ZV input shaping technique includes two additional conditions that must be completed and that will help us work out the values of amplitudes and delays:

$$\sum_{i=1}^{p} A_i = 1, \quad A_i > 0 \tag{3.44}$$

With all this information, the solutions for the amplitudes and delays can be found:

$$A_i = \frac{a_i}{(1 + e^{-\pi\xi/\sqrt{1-\xi^2}})^{p-1}}, \qquad i = 1..p \tag{3.45}$$

$$t_i = T(i-1), \qquad i = 1..p \tag{3.46}$$

Where p is the number of impulses to be used in the shaper and a_i is the ith coefficient of the following polynomial expression:

$$(1 + e^{-\pi\xi/\sqrt{1-\xi^2}})^{p-1} \tag{3.47}$$

The number p of impulses to be used can be decided by trial and error, starting from two and increasing the number until no improvement is observed no matter how many more impulses are used.

Finally, the input shaper can be represented in a block diagram as depicted in Figure 3.12.

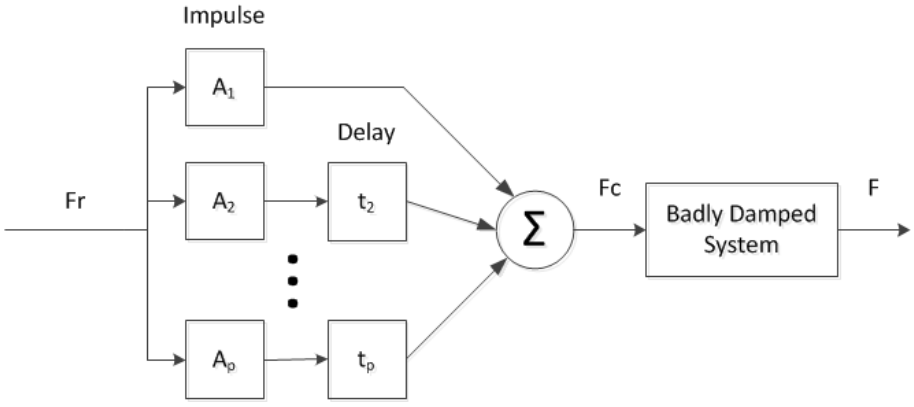

Figure 3.12. *Block diagram of an input shaper designed with the ZV input shaping technique.*

Of course, since the system needs to be modeled as an approximation to a second order system the dynamic compensation might not be perfect. However, the elimination or mitigation of the overshoot, the reduction of the settling time and a considerable reduction of the oscillations are expected as a result of the implementation of this input shaping technique.

3.2. Software

This section introduces the software used in Chapter 4 to Chapter 6 for the measurements and the design of the controller. These include SolidWorks, MATLAB, Simulink and XPc-Target.

3.2.1. SolidWorks

SolidWorks is a computer-aided design software for mechanical design developed by SolidWorks Corp. SolidWorks makes the design of models and assemblies possible from a parametric feature-based approach. SolidWorks has been used for the design of the test platform described later in Section 3.3.8.

3.2.2. MATLAB

MATLAB is a mathematical software created by Mathworks that offers an integrated development environment (IDE) with its own programming language, language M. Among its most important features one can find matrix manipulation, plotting of data and functions, implementation of algorithms, creation of graphical user interfaces (GUI) and communication with other hardware devices and/or programs that use other programming languages, such as C, C++ or Java. Several toolboxes can be added to MATLAB to extend its functions and capabilities. MATLAB has been used for the analysis of the data measured and the necessary calculations in Chapter 4 to Chapter 6.

3.2.3. Simulink

Developed by MathWorks, Simulink is an environment for simulating and designing multidomain dynamic and embedded systems. It can be found integrated in MATLAB, offers an ample range of tools for algorithms and the possibility to analyze and visualize simulations and allows the defining of signals, parameters and other testing data, among other features.

Simulink was used for the creation of the input signals and the models required for the characterization in Chapter 5 and the implementation of the designed control schemes in Chapter 6.

3.2.4. XPc-Target

XPc-Target is an additional toolbox for MATLAB created by MathWorks consisting of a real-time operating system and a library of data-acquisition blocks for Simulink that enables the simulation and testing of Simulink models on a target computer for a variety of real-time testing applications, such as control prototyping given its ability to handle

complex control schemes with relatively high frequencies. XPc-Target has been used for real-time testing and data acquisition in Chapter 4 to Chapter 6.

3.3. Hardware

This section presents the devices, actuator and tools used in the experiments of Chapter 4 to Chapter 6. These include a piezo amplifier, a measurement board, an actuator, a force sensor, a displacement sensor, different power supplies, an amplifying circuit and a custom-built platform.

3.3.1. Piezo Amplifier

The piezo amplifier used in the experiments carried out during the thesis work is a Piezo Systems Inc. EPA-102. Its most relevant characteristics have been included in Table 3.1.

Table 3.1. *Specifications of the piezo amplifier EPA-102, from Piezo Systems Inc.*

Maximum Input Voltage	± 10 V
Voltage Gain	0 to 20
Frequency Range	DC to 300 kHz
Maximum Output Voltage	± 200 V
Maximum Output Current	± 200 mA
Output Power	40 W

For more information, refer to the corresponding data sheet [36].

3.3.2. Measurement Board

Data acquisition in all the experiments has been managed by a Measurement Computing A/D board, the model being PCI-DAS 1001. Some of the most important characteristics have been included in Table 3.2.

Table 3.2. *Specifications of the measurement board PCI-DAS1001, from Measurement Computing.*

Resolution	12 bits
Number of Channels	8 Differential or 16 Single-Ended (Software selectable)
Maximum Input Range	± 10 V
Maximum Output Range	± 10 V
Polarity	Unipolar/Bipolar (Software selectable)

More information can be found in the corresponding data sheet [29].

3.3.3. Actuator

The piezoelectric actuator studied is a PSt 150/5/100 VS10 piezoelectric stack from Piezomechanik GmbH. Table 3.3 shows some of the most relevant characteristics of the actuator.

Table 3.3. *Specifications of the piezoelectric stack PSt 150/5/100 VS10, from Piezomechanik GmbH.*

Maximum Load Force	800 N
Maximum Tensile Force	150 N
Maximum Input Voltage	150 V
Maximum Stroke	130/100 μm
Resonance Frequency	10 kHz
Output Power	40 W

For more information, including the physical dimensions of the actuator, refer to the corresponding data sheet [37].

3.3.4. Force Sensor

The force sensor used in the majority of the experiments carried out during the thesis work is a LCM302-1KN load cell from Omega Engineering Inc. The parameters of this force sensor have been included in Table 3.4.

Table 3.4. *Specifications of the load cell LCM302-1KN, from Omega Engineering Inc.*

Maximum Load Force	1 kN
Excitation Voltage	5 to 15 Vdc
Output	1 mV/Vexc
Accuracy	± 0.5 %
Safe Overload	150 %

More information, including the physical dimensions of the load cell, can be found in the corresponding data sheet [34].

3.3.5. Displacement Sensor

A displacement sensor was needed for the test carried out in Section 5.3 to find the origin of an anomaly observed in the load cell measurements. A MEL M5L/2 laser sensor from Microelectronik GmbH was selected among different options, and its characteristics can be found in Table 3.5.

Table 3.5. *Specifications of the laser sensor MEL M5L/2, from Microelectronik GmbH.*

Measurement Range	± 0.25 mm
Stand-Off Distance	24 mm
Linearity Error	2 μm
Resolution	0.1 μm
Voltage Output	± 10 Vdc

For more information, including the physical dimensions of the actuator, refer to the corresponding data sheet [30].

3.3.6. Power Supplies

In Section 4.1 four different power supplies are tested in order to find out which one is the most appropriate for supplying the load cell. The four power supplies tested are:

- B403, from Oltronix Industrial Power Supplies [35].
- 6303DS, from Topward Electric Instruments Co. [62].
- IPS601A, from ISO-TECH [17].
- NP7-12, from Yuasa Batteries Inc. [66].

3.3.7. Amplifier Circuit

The signal provided by the load cell selected was initially too low and noisy, resulting in a rather low resolution in the measurements.

For this reason, an amplifier circuit was designed and built based on the INA118 precision, low power instrumentation amplifier from Texas Instruments, as expounded in Section 1 where further details on the complete design can be found. Some of the parameters of the chosen amplifier can be seen in Table 3.6.

Table 3.6. *Specifications of the INA118 amplifier, from Texas Instruments.*

Gain	1 to 10000
Input Type	Bipolar
Maximum Non-Linearity	± 0.002 %
Voltage Supply	2.7 to 36 V

Further information on the characteristics of the amplifier can be found in the data sheet [7].

3.3.8. Test Platform

The execution of this thesis work required the design and manufacture of a test platform. Such platform would be used to hold the actuator and make possible its

movement, house the load cell and permit the positioning of the metal plates containing paper fibers under the actuator.

A first approach was based on the platform designed in a previous work [68], consisting on a three-legged structure supporting a positioner in charge of sustaining and transport the actuator.

At first the use of a commercial micropositioner was considered to achieve the vertical movement of the actuator, but a thorough search revealed that very few micropositioners available would be able to withstand the maximum load provided by the actuator, and those that could were considerably expensive. A custom-built positioner was conceived as an alternative consisting of a fine threaded screw that goes through the aforementioned structure, of which the end is united to an element that will be sustaining the actuator thanks to a ball bearing. Thus, the turning of the screw would be transformed into the vertical movement of the actuator.

A rough draft of this first concept integrating the custom-built positioner can be seen in Figure 3.13.

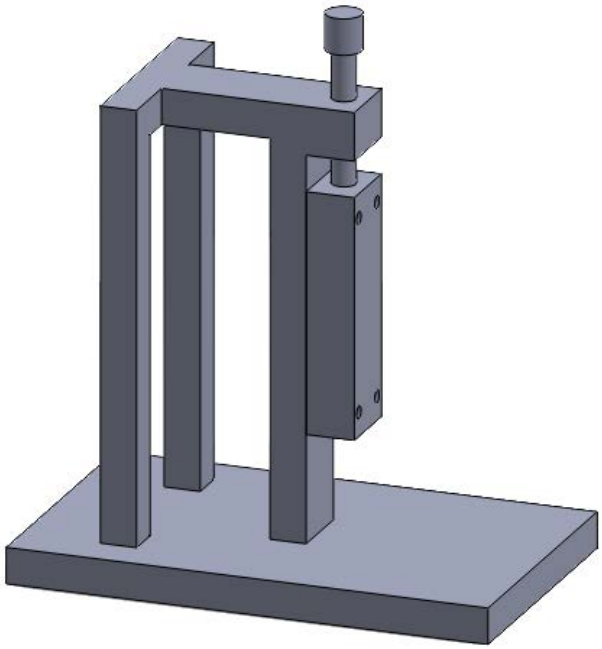

Figure 3.13. *Draft of the initial approach considered, done with SolidWorks 2011.*

This initial concept was soon discarded for several reasons, among which the most important are the overturning moment the three-legged structure would be subjected to when using the actuator and the unequal distribution of forces throughout the whole design.

In an effort to solve these issues a new scheme was devised. The three-legged frame was replaced by a two-legged one that provided more symmetry, in which center the positioner and the actuator were placed, and therefore would limit the overturning moment and allow a better distribution of forces.

The positioning mechanism from the previous design was preserved and improved by shaping the legs so that they also serve as rails to help the vertical movement of the

element sustaining the actuator and prevent it from turning along with the screw. The sustaining element for the actuator and the actuator were to be joined by a headless screw, since the actuator provided a threaded hole on its rear. Also, a F8-16M thrust ball bearing from SUPbearing Co. [58] was definitely selected for the device. This second design can be seen in Figure 3.14.

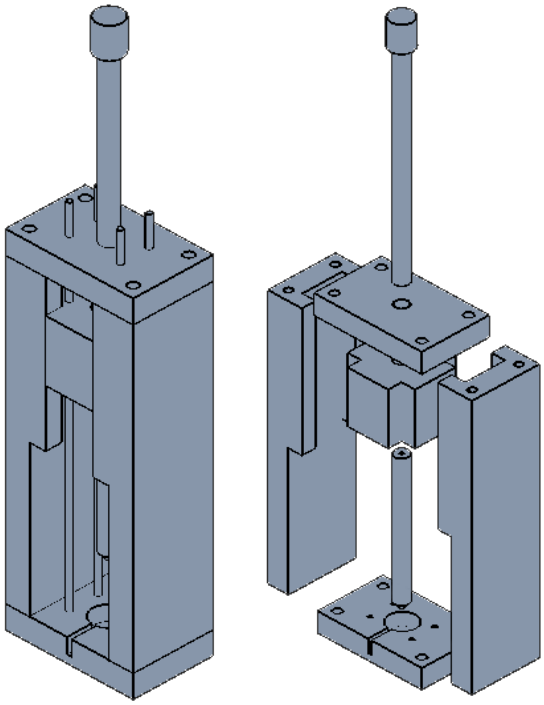

Figure 3.14. *SolidWorks model of the final design. Left, an image of the assembled platform. Right, an image of the disassembled platform for a better understanding on how it operates.*

Two additional features can be observed in the latest conception. On one hand, a small space has been included in the base and right below the actuator where the load cell can be comfortably placed. On the other, four metal rods passing through the whole platform have been included to help fix the metal plates with the paper fibers.

Detailed drawings for all the pieces forming the platform including all the dimensions can be found in Appendix A: Designs of the Test Platform.

4. Load Cell Signal Processing

The load cell selected for the tests to be carried out during this thesis work is the LCM302-1KN, from Omega Engineering, Inc. Its price, size, measuring range and overall characteristics [34] made it one of the most suitable options. However, considering the output to excitation voltage ratio, the maximum excitation voltage possible and the measuring range it can be inferred that the maximum sensitivity of the device will be $12.66\ \mu V/N$.

Such a low sensitivity would mean that really low levels of noise should be present in order to have a good resolution in the measurements. Small levels of noise are not likely to be found without amplification and/or filtering of the signal, so both measures will be essential in order to acquire utilizable results. When amplifying a signal we cannot forget that we will also be amplifying the noise of the system. While filtering will be later proposed, noise can also be limited by a careful initial selection of the different components that belong to both the system and the amplifying circuit.

Thus, Section 4.1 will deal with the selection of a power supply that provides the minimum noise possible among different possibilities. This will be followed by Section 4.2, which proposes a circuit designed for amplification and filtering of the signal. Last, conclusions will be drawn in Section 4.3.

4.1. Selection of the Power Supply

The first step consisted on choosing a power supply for the load cell that caused the lowest level of noise possible. Three different power supplies and a 12 V battery, as listed in Section 3.3.6, were tested to sustain the load cell. In Figure 4.1 a comparison between the signals originating from the load cell when using the different power supplies is shown. The noise levels measured in each power supply are expressed in Table 4.1 as the standard deviation of the signal during a certain interval. As a side note, the first few tests in this section were carried out on a LCM302-500N load cell [34] instead of on a LCM302-1KN given that at the time the latter was unavailable. However, since the only difference was the measuring range of each sensor the results could be extrapolated to the latter when it was available.

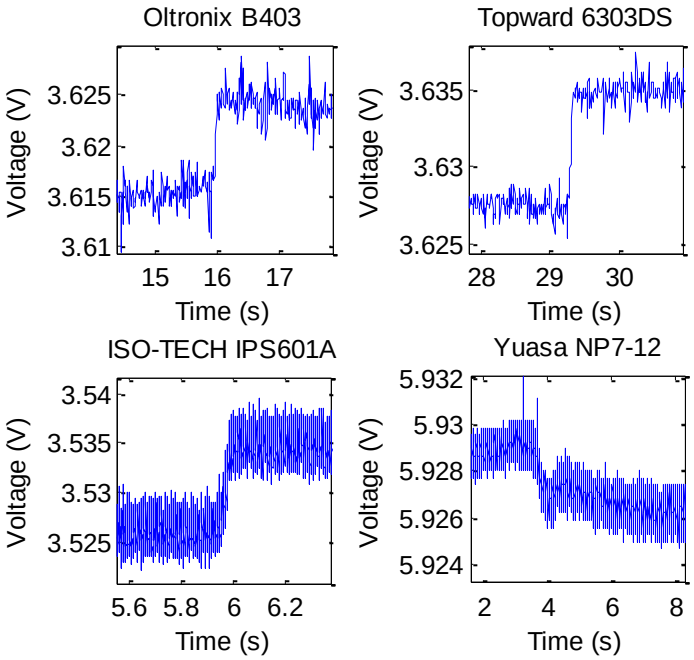

Figure 4.1. *Responses of the load cell against manually applied random forces when using different power supplies.*

Table 4.1. *Noise levels measured from the load cell when using different power supplies. The noise values are calculated as the standard deviation in the static parts of the signals.*

	Power Supply			
	Oltronix	**Topward**	**ISO-TECH**	**Yuasa**
Noise (mV)	1.3	0.74	1.1	0.384

As expected, the 12 V battery (NP7-12 from Yuasa Batteries) is the power supply that provides the lowest level of noise. At first the use of two 12 V batteries in series along with a 15 V regulator was proposed in order to achieve the highest sensitivity possible from the load cell, but the inclusion of said regulator would be another source of undesired noise in the system. In addition, the voltage provided by the battery is considered to be stable enough to be treated as a constant value during the tests and high enough to have a good sensitivity value after the amplification.

The voltage excitation was measured before starting every experiment considering that, as a matter of fact, the voltage provided is not 12 V but a rather close value. The average of all of these values was then calculated, resulting in 12.1 V.

4.2. Amplification and Filtering

As previously mentioned, the sensitivity of the load cell is quite low, meaning that even with a low noise power supply the noise might be too high to have a good resolution. At

this moment the resolution, understood as the ratio between the noise and the sensitivity, can be calculated to be 37.65 N, as seen in Equation (4.1).

$$Resolution = \frac{Noise}{Sensitivity} = \frac{0.384\ mV}{10.212\ \mu V/N} = 37.65\ N \tag{4.1}$$

To illustrate the lack of resolution due to high noise and low sensitivity, the output of the load cell in a test in which a 1 kg weight was used is shown in Figure 4.2. Note that the results provided from now on have been acquired from the LCM302-1KN load cell.

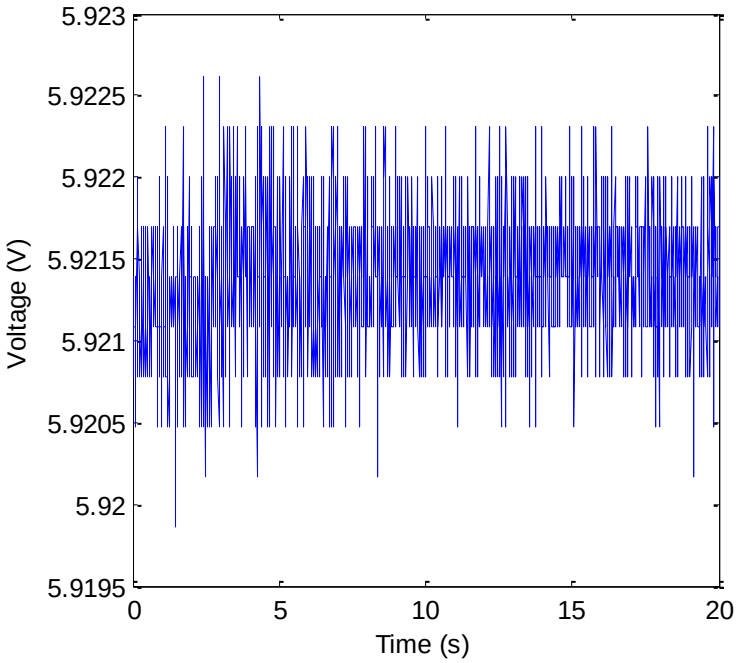

Figure 4.2. *Response measured from the load cell when manually placing a 1 kg weight.*

Observing the amplitude of the response and comparing it with the noise levels one can easily infer that amplification is absolutely necessary in order to achieve a good resolution in the measurements, by increasing the sensitivity while keeping low the noise levels. Also, note the high quantization of the noise, causing an important loss of information concerning the noise of the signal. Another advantage related to the amplification to be applied to the signal will be the reduction of the quantization error.

An auxiliary circuit was then proposed and built to amplify the output of the load cell, and therefore improve the resolution. The main element for this circuit is an INA118 precision, low power instrumentation amplifier from Texas Instruments [36], characterized by the low noise caused in the amplification. The gain can be modified by means of an external resistor, and the output is referred to a reference voltage. The reference voltage was set to zero by grounding the port. The layout of the initially proposed amplifying circuit can be seen in Figure 4.3.

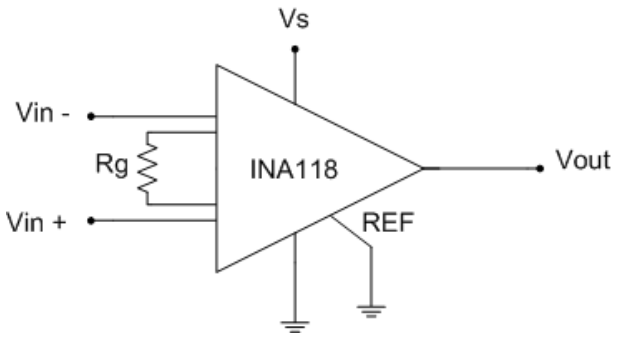

Figure 4.3. *Layout of the amplifying circuit initially proposed.*

A gain of 1000 was considered for the amplifier, which would require a gain resistor of 50.05 Ω according to the formula provided in the specifications of the instrumentation amplifier and expressed in Equation (4.2).

$$R_G = \frac{50\ k\Omega}{G-1} = \frac{50\ k\Omega}{1000-1} = 50.05\ \Omega \tag{4.2}$$

Instead, a gain resistance of 51.1 Ω was selected for the circuit since it was the closest one available, leading to a theoretical amplification of 979.473 as seen in Equation (4.3).

$$G = 1 + \frac{50\ k\Omega}{R_G} = 1 + \frac{50\ k\Omega}{51.1\ \Omega} = 979.473 \tag{4.3}$$

In addition to the amplification, analog filtering was considered for noise reduction and the improvement of the resolution. Two measures have been taken to reduce the noise by means of analog filtering.

First, a low pass filter was applied to the load cell output. The cutoff frequency was decided to be 10 kHz, so considering the output impedance, 352.9 Ω according to the specifications of the load cell, a 45 nF capacitor was needed for the filter (see Equation (4.4)).

$$C = \frac{1}{2\pi \cdot R_{out} \cdot f_{cutoff}} = \frac{1}{2\pi \cdot 352.9\ \Omega \cdot 10\ kHz} = 45\ nF \tag{4.4}$$

A 47 nF capacitor, being the closest one available, was used instead, meaning that the actual cutoff frequency will be 9.59 kHz (as seen in Equation (4.5)), a value close enough to the filter originally proposed.

$$f_{cutoff} = \frac{1}{2\pi \cdot R_{out} \cdot C} = \frac{1}{2\pi \cdot 352.9\ \Omega \cdot 47\ nF} = 9.5956\ kHz \tag{4.5}$$

The second step taken involves bypassing the power supply lines feeding the operational amplifiers to limit the effect of the noise from the power supply on their outputs [26]. Two capacitors have been added in parallel to each of connections to the positive and negative terminals of the operational amplifiers. The purpose of these

capacitors is to filter the high and low frequencies of the signal originating from the battery: a 10 µF electrolytic bulk capacitor helps provide low frequency instantaneous current, while a 100 nF ceramic capacitor provides high frequency instantaneous current.

The implementation of the low pass filter and the bypass capacitors to the originally designed amplifying circuit is depicted in Figure 4.4.

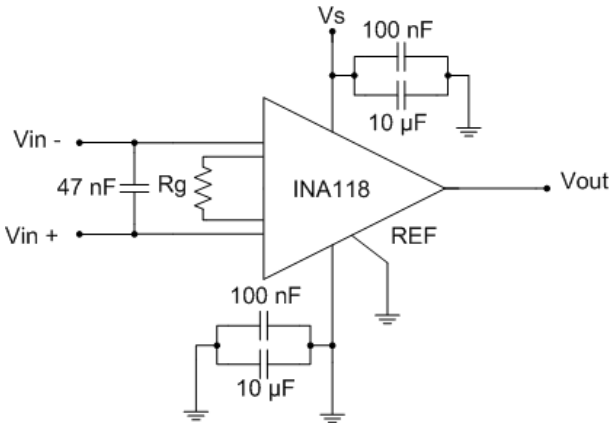

Figure 4.4. *Layout of the final amplifying circuit, including the analog filtering measures.*

The amplifying circuit along with the analog filtering measures was then implemented to the load cell and tests with different weights ranging from 100 g to 1 kg were carried out to test the improved resolution of the measurements. In Figure 4.5 the result when using a 1 kg weight is shown.

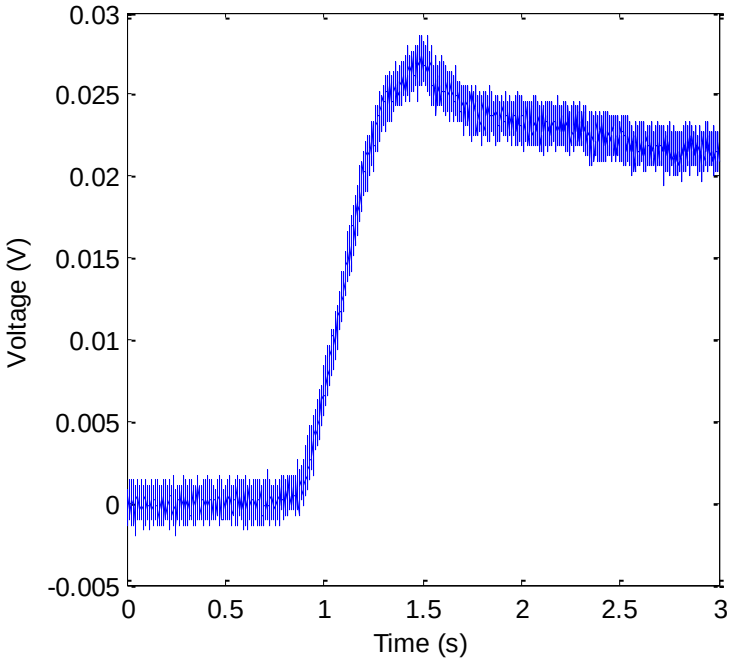

Figure 4.5. *Response measured from the load cell when manually placing a 1 kg weight, after the implementation of the amplification and filtering.*

An obvious and considerable improvement can be observed with respect to the result seen in Figure 4.2. Quantization can still be noticed in the figure, but the effect has been substantially reduced. Noise can now be measured to be 0.578 mV, while the sensitivity has been increased to 10.003 mV/N taking into consideration both the amplification and the voltage supplied by the battery. Therefore, the resolution of the measurements will finally be 0.0578 N, as expressed in Equation (4.6).

$$Resolution = \frac{Noise}{Sensitivity} = \frac{0.578\ mV}{10.003\ mV/N} = 0.0578\ N \tag{4.6}$$

4.3. Conclusion

The measures taken in this section have led to an enhancement of the overall resolution. Thus, the reduction of noise from the power supply, the amplification and the analog filtering have improved the initial resolution of 37.65 N to a final value of 0.0578 N.

The processing of the signal from the load cell achieved in this chapter will lead to more precise measurements in the subsequent chapters, and consequently to a more precise and better designed control.

5. Characterization of the Actuator

The characterization process is essential and comprises several tests with the aim to fully describe the behavior of the system in different situations. The data collected through the characterization tests will later be of use for the design of the different control schemes.

Three phenomena will be analyzed in this chapter: Section 5.1 will deal with hysteresis, Section 5.2 with creep or drift and finally Section 5.3 will be destined to describe the vibrations of the system. Section 5.4, concludes this chapter.

5.1. Hysteresis

The first non-linearity to be studied will be the hysteresis. As previously explained in the introductory chapter, hysteresis can be observed when using an alternately increasing and decreasing input signal. Such an input signal will result in different output values depending on if the input is increasing or decreasing, forming a loop when plotting the input values against the output values.

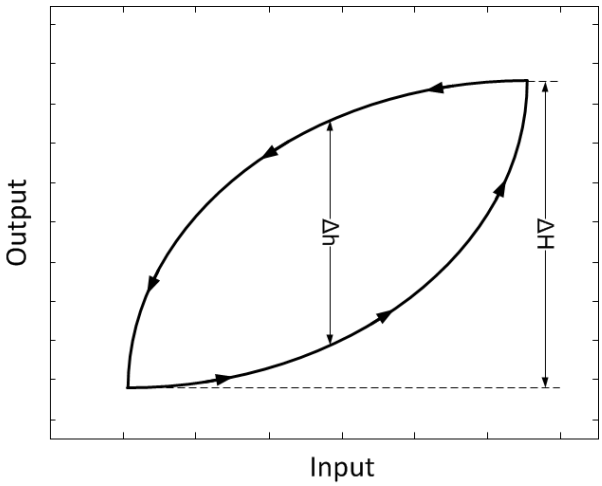

Figure 5.1. *Hysteresis curve and parameters needed for the calculation of the maximum hysteresis.*

The maximum hysteresis has been calculated as follows:

$$Max.Hysteresis = \frac{\Delta h}{\Delta H} \cdot 100 \tag{5.1}$$

Where Δh is the maximum difference between output readings for a given measured point and ΔH is the full output range. These parameters are graphically represented in Figure 5.1.

Several tests were carried out using triangular signals with different frequencies varying from zero to the maximum allowed input, since we are particularly interested in the maximum hysteresis of the actuator. Using a range of frequencies will allow us to observe the rate-dependency of the hysteresis. The results obtained when using different frequencies ranging from 0.1 Hz to 100 Hz are shown in Figure 5.2, while Table 5.1.

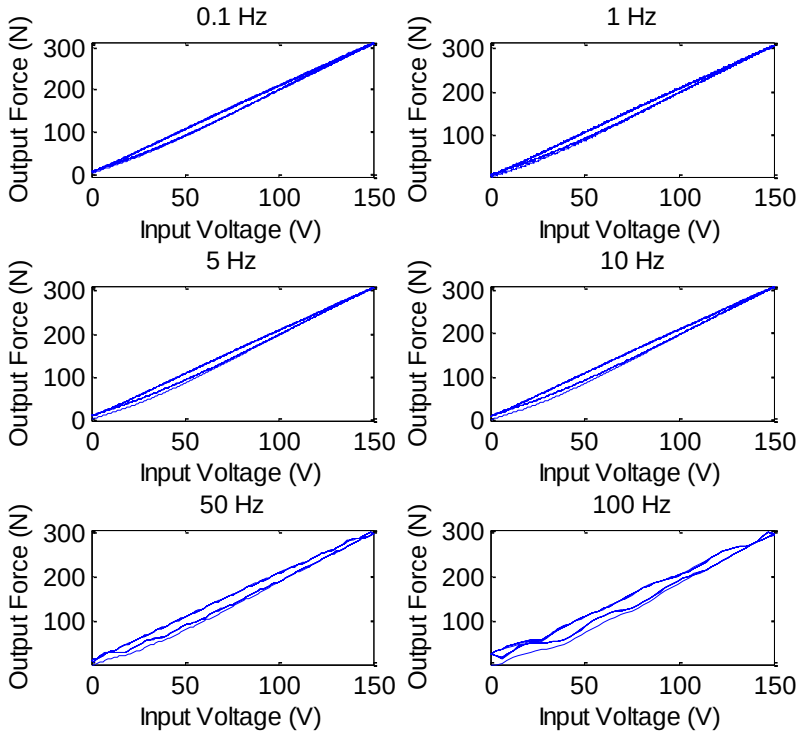

Figure 5.2. *Hysteresis curves when using a triangular periodic input with the maximum amplitude recommended and frequencies ranging from 0.1 to 100 Hz.*

Table 5.1. *Maximum hystereses calculated when using a triangular periodic input with the maximum amplitude recommended and frequencies ranging from 0.1 to 100 Hz.*

	Frequency (Hz)					
	0.1	**1**	**5**	**10**	**50**	**100**
Max. Hysteresis (%)	5.63	5.68	5.72	5.9	8.37	11.24

From these results we can infer that the maximum static hysteresis (or hysteresis at low frequencies) can be considered to be 5.63 %. Also, the rate-dependency of the hysteretic behavior of the actuator becomes evident when using higher frequencies, causing the hysteresis to increase. In addition, at higher frequencies the behavior of the actuator seems to become erratic, even if its resonance frequency is, according to the specifications [37], 10 kHz.

5.2. Creep

The second non-linearity that will be analyzed is drift or creep. Drift or creep can be observed as a deviation from a steady-state value of the output when applying an input over a prolonged period of time.

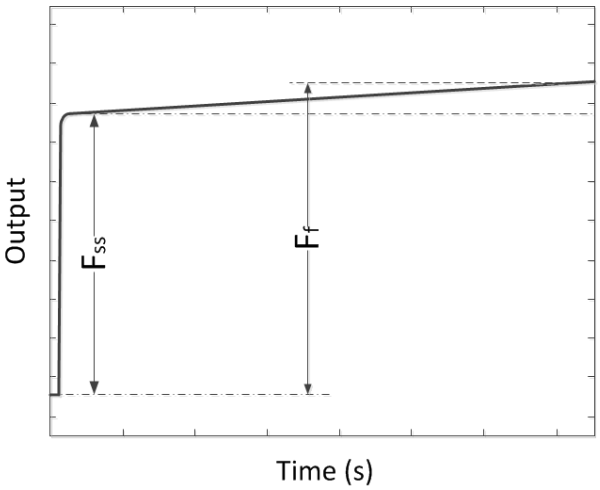

Figure 5.3. *Creep and parameters needed for its quantification.*

Creep has been calculated according to the following formula:

$$Creep = \frac{F_f - F_{ss}}{F_{ss}} \cdot 100 \tag{5.2}$$

Where F_{ss} is the steady-state value of the signal and F_f the final value after a given period of time. These parameters are graphically represented in Figure 5.3.

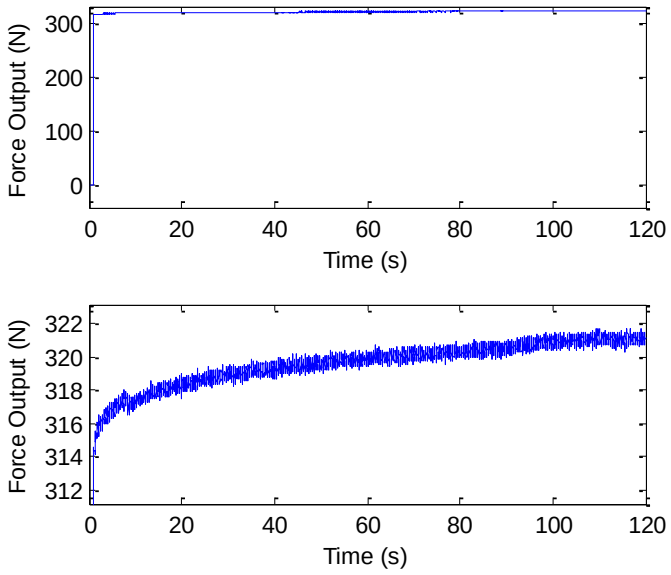

Figure 5.4. *Step response after 120 s (top) and detail of the creep measured from it (bottom).*

In order to measure the creep the maximum input voltage was applied during a period of 120 s. The response of the system can be seen in Figure 5.4, from which drift can be measured to be 2.36 %.

5.3. Vibrations

The last object of study in this characterization process is the dynamic behavior of the actuator. When subjecting a system to a sudden change in the input overshoot and oscillations may appear.

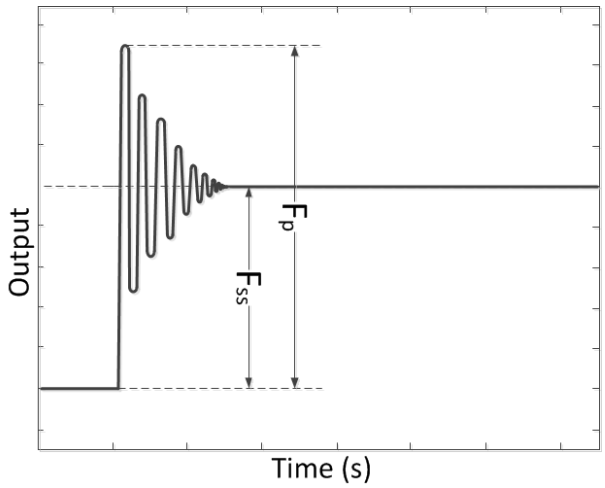

Figure 5.5. *Oscillations suffered by a badly damped system and parameters needed for the calculation of the overshoot.*

Overshoot has been calculated as follows:

$$Overshoot = \frac{F_p - F_{ss}}{F_{ss}} \cdot 100 \tag{5.3}$$

Where F_{ss} is the steady-state value of the signal and F_p its peak value. These parameters are graphically represented in Figure 5.5.

Measuring the step response while using a high sampling frequency will allow us to observe the dynamic behavior. Several tests were carried out using different values for the input voltage, the results being shown in Figure 5.6.

When using an input voltage of 20 V the overshoot can be measured to be 25.92 %. Per contra, an unexpected phenomenon takes place when using input voltages over a certain value, measured by the load cell as a notch that causes an important loss of information. Since the origin of the anomaly is completely unknown, a set of different tests was devised to help find the cause.

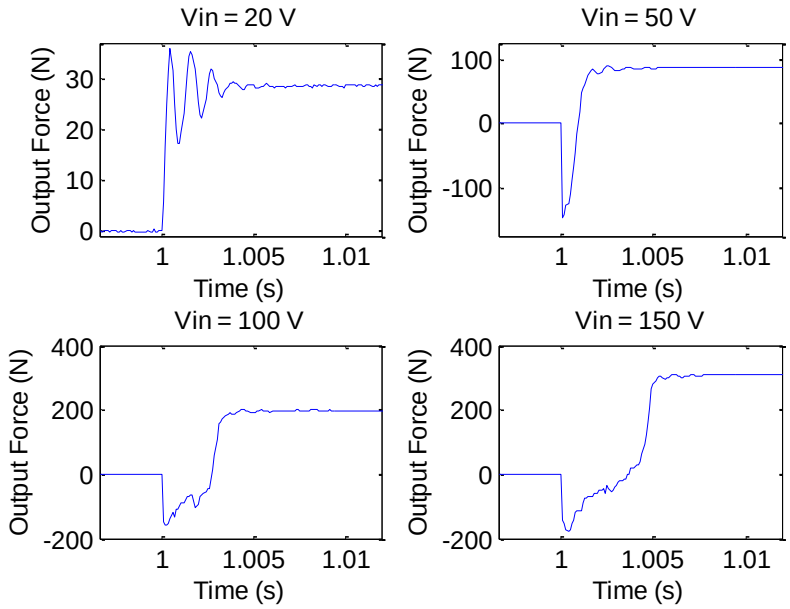

Figure 5.6. *Step responses when using different input values. Observe the unexpected appearance of notches in three of the four plots.*

The first hypothesis supposes a possible internal interference in the measurement board, since it is the one in charge of providing the input voltage for the actuator and receiving the output from the load cell. In order to test this hypothesis a new measurement board was added to the set-up, in order to be able to provide the input for the actuator with one measurement board while the other is in charge of the measurements. However, this hypothesis was proven to be erroneous as shown in Figure 5.7, where the anomaly is again present when using a high enough input voltage.

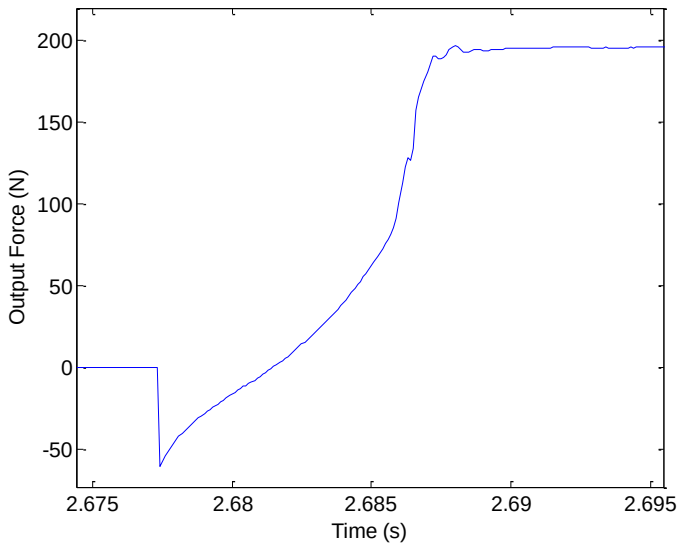

Figure 5.7. *Step response when using a different measurement board to providean input signal of 100 V.*

A second hypothesis was proposed, which assumed that this anomaly was due to a malfunction of the actuator when using certain input voltages, possibly a bounce-back behavior. This hypothesis was tested by measuring the displacement of the tip of the actuator by means of a laser sensor. The MEL M5L/2 laser sensor [30] was used for this purpose. Several tests were run using different input voltages and the results are shown in Figure 5.8.

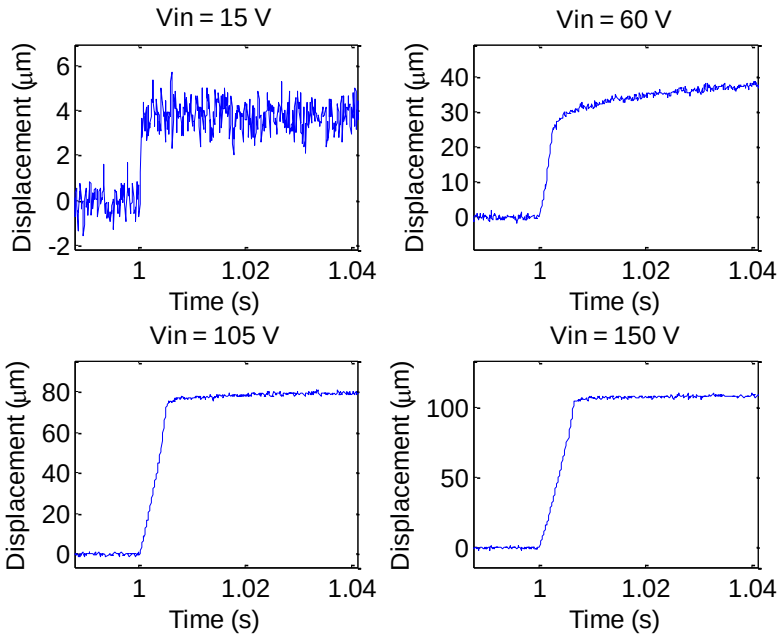

Figure 5.8. *Step responses when using different input values. Note the absence of the aforementioned phenomenon in the displacement measurements.*

The results prove that this last assumption is also wrong, but they help propose and support one last hypothesis. Thus, the anomaly was proposed to be attributed to electromagnetic interferences coming from the actuator affecting the load cell measurements. Tests in which there was no contact at all between the actuator and the load cell were carried out using the maximum step input possible and placing the load cell at different distances from the actuator with the objective of confirming this premise. Two of the results are displayed in Figure 5.9.

From these results we can infer that not only the phenomenon is present even when there is no contact between the load cell and the actuator, but also that its magnitude is decreased when moving the load further away from the actuator. Therefore, the hypothesis is proven and the origin of the anomalies has been identified.

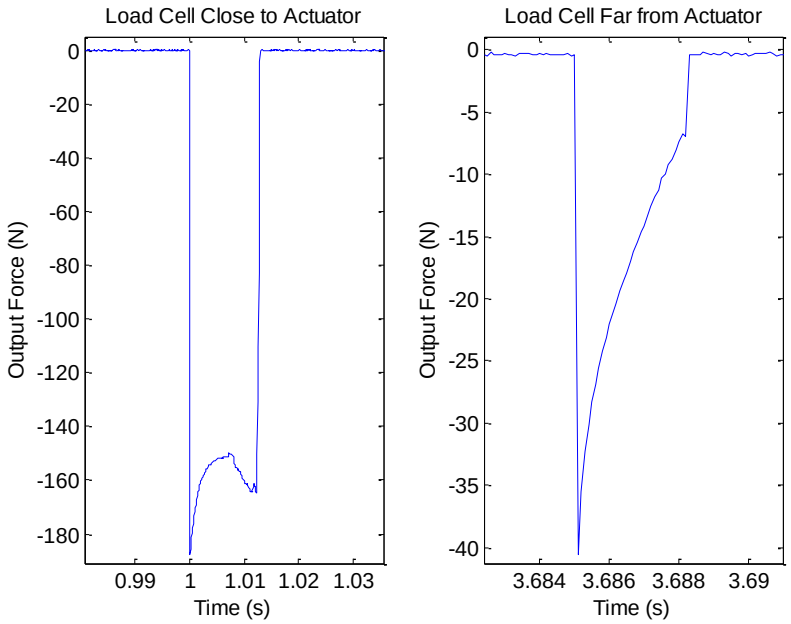

Figure 5.9. *Measurement of the anomaly when there is no contact between actuator and load cell at different distances.*

Some solutions were proposed and tested in order to protect the load cell from the electromagnetic interferences. However, since the contact between the actuator and the load cell is required none of them were able to completely rid the system of the anomaly and were therefore discarded.

Given this situation, the characterization of the dynamic behavior will be done using the results obtained at low input voltages, where the effect of the interferences is non-existent, considering that the dynamic behavior should theoretically stay the same over the whole range of values to be measured.

5.4. Conclusion

The three parameters measured within the last subsections have been gathered in Table 5.2, which can be seen below.

Table 5.2. *Parameters measured for the characterization of the actuator.*

Maximum Static Hysteresis	5.63 %
Creep After 120 s	2.36 %
Overshoot	25.92 %

Except for the overshoot, which in any case was measured only for low input magnitudes due to electromagnetic interferences between the actuator and the sensor, the other two phenomena have been measured to be considerably low. Nevertheless, the compensation techniques proposed in Section 3.1 will try to mitigate or even rid the system of both non-linearities and undesired vibrations in the next chapter, in order to achieve the best performance possible from the actuator.

6. Force Control

This chapter focuses on the objective of this thesis: the implementation and validation of an open-loop force control scheme to a piezoelectric actuator. As it was mentioned in Section 2.3, force control for piezoelectric actuators is still a relatively young subject of study but much needed for manipulation processes. In addition, designing an open-loop scheme could lead to possible further miniaturization of the system. The compensation techniques presented in this chapter are already existing approaches to open-loop displacement control for piezoelectric actuators, and their performance will be tested when applied to force control instead.

Section 6.1 describes the experimental setup needed for the subsequent tests. The implementation and verification of the hysteresis, creep and vibration compensations will be dealt with in Section 6.2, Section 6.3 and Section 6.4 respectively. This will be followed by Section 6.5, destined to the verification of the performance of the complete control scheme. In addition, the tracking performance will be analyzed in Section 6.6. Last, Section 6.7 will present the conclusions drawn from the results collected within the previous sections.

6.1. Experimental Setup

The experimental setup consists of the actuator, the custom-built test platform, the force sensor, the battery to supply the force sensor, the measurement board, the piezo amplifier and the control software. An illustrative diagram portraying these elements and the connections between them is shown in Figure 6.1.

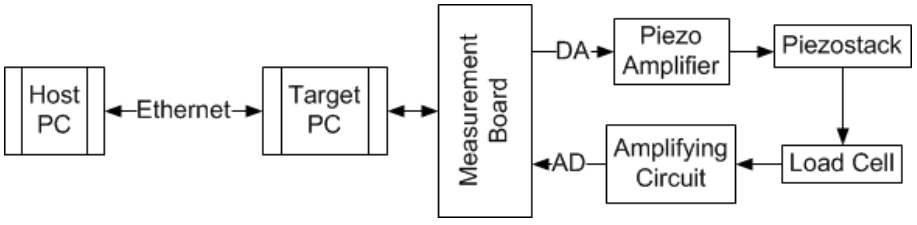

Figure 6.1. *Diagram of the experimental setup.*

Before starting any test an offset of at least 0.5 V or 50 N needs to be reached by lowering the actuator and pressing it against the load cell, which helps secure the structure and prevents the actuator from losing contact with the load cell during the tests. This will eliminate unexpected vibrations and random behavior from the actuator.

6.2. Hysteresis Compensation

The compensation of the hysteretic non-linearity will be approached by formulating an inverse model of the hysteresis measured from the actuator during the characterization process, which will later be implemented in series with the actuator.

The inverse model will be calculated and implemented in Section 6.2.1, while Section 6.2.2 will deal with the analysis of the performance of the compensation designed.

6.2.1. Implementation

As explained in Section 3.1.1, the design of the hysteresis compensation proposed begins with building a model for the static hysteresis using the data collected during the characterization process. When modeling hysteresis through different methods some authors propose using the hysteresis curve obtained when applying the maximum input value periodically [42], while others resort to the hysteresis curve resulting from a periodic input with varying amplitude [8], [19]. Thereby, two different approaches for the construction of the model have been taken, of which the results will be shown and compared in the next subchapter.

The first approach for the modeling was based on the hysteresis loop obtained when using a periodic triangular signal with amplitude equal to the maximum input and frequency of 0.1 Hz, since the aim is to model the static hysteresis. The input and output of the system under these conditions have been illustrated in Figure 6.2, while Figure 6.3 depicts the hysteresis curve resulting from the test. Maximum hysteresis can be now measured to be 5.5 %.

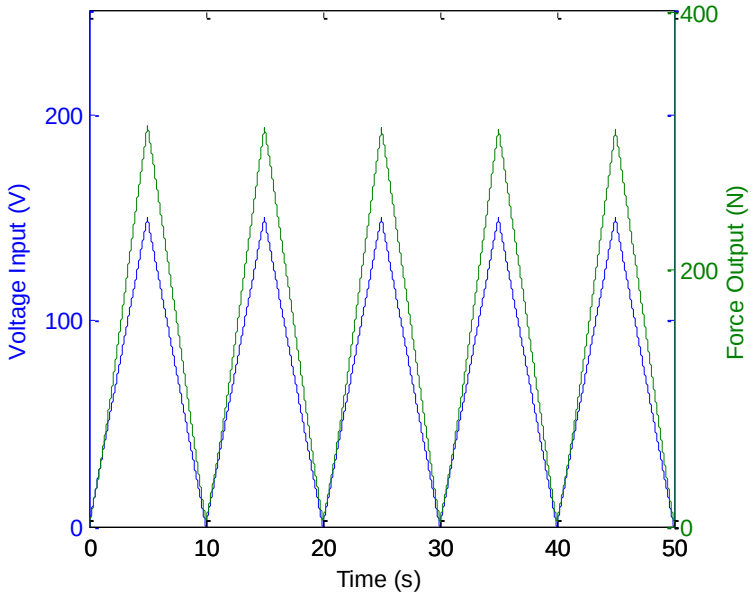

Figure 6.2. *Evolution of input (in blue) and output (in green) when using a periodic triangular signal with maximum amplitude and frequency of 0.1 Hz as input.*

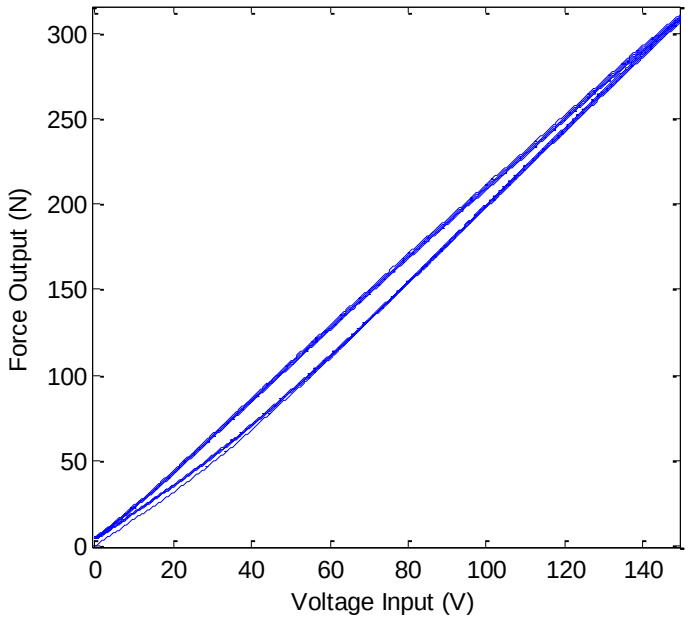

Figure 6.3. *Hysteresis curve obtained when using a periodic triangular signal with maximum amplitude and frequency of 0.1 Hz as input.*

On the other hand, the second approach proposed a periodic triangular signal with varying amplitude and frequency of 0.1 Hz as input to model the static hysteresis. The input and output of the system under these conditions have been pictured in Figure 6.4, while Figure 6.5 shows the hysteresis curve resulting from the test. Maximum hysteresis can be now measured to be 6.17 %.

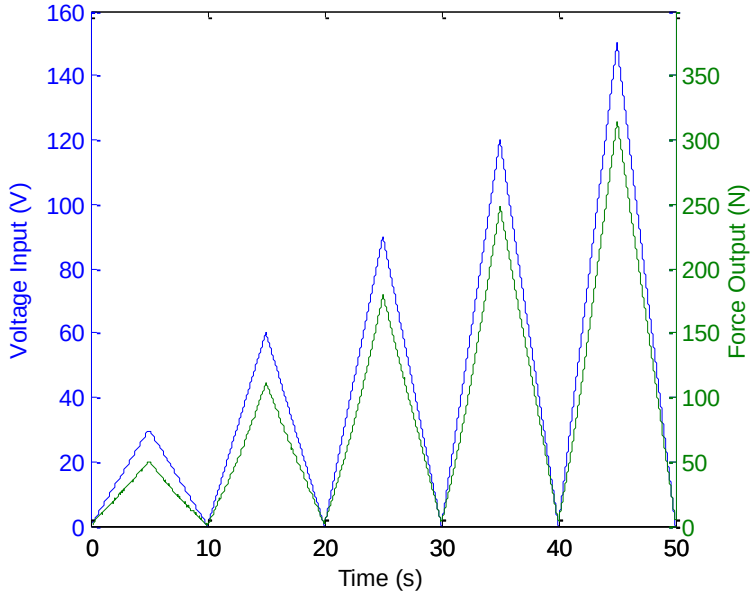

Figure 6.4. *Evolution of input (in blue) and output (in green) when using a periodic triangular signal with varying amplitude and frequency of 0.1 Hz as input.*

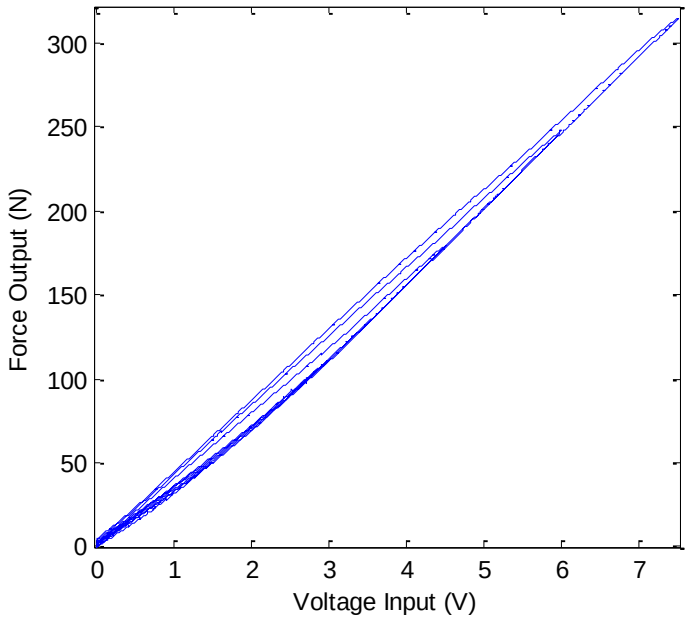

Figure 6.5. *Hysteresis curve obtained when using a periodic triangular signal with varying amplitude and frequency of 0.1 Hz as input.*

The data from the hysteresis curves can now be used to determine the parameters of the direct and inverse model. At this stage it is important to note that since the input of the actuator is unipolar instead of bipolar the number of one-sided dead zone operators will be $m + 1$ instead of $2m + 1$.

As it was stated in Section 3.1.1, one should begin with a reduced number of backlash and one-sided dead zone operators and develop models iteratively increasing their order in each iteration until acceptable matching results are obtained.

The identification for the first set of data was started with low order parameters $n = 2$ and $m = 1$, and the parameter ε was set to be 0.01. After several iterations, a model with $n = 12$ and $m = 1$ was found to be accurate enough to the measured model, as observed in Figure 6.6. It was observed that increasing neither *n* nor *m* would not improve the identified model. In addition, since the number of one-sided dead zone operators is so low their contribution to the model is rather small and the hysteresis loop can be considered to be practically symmetric.

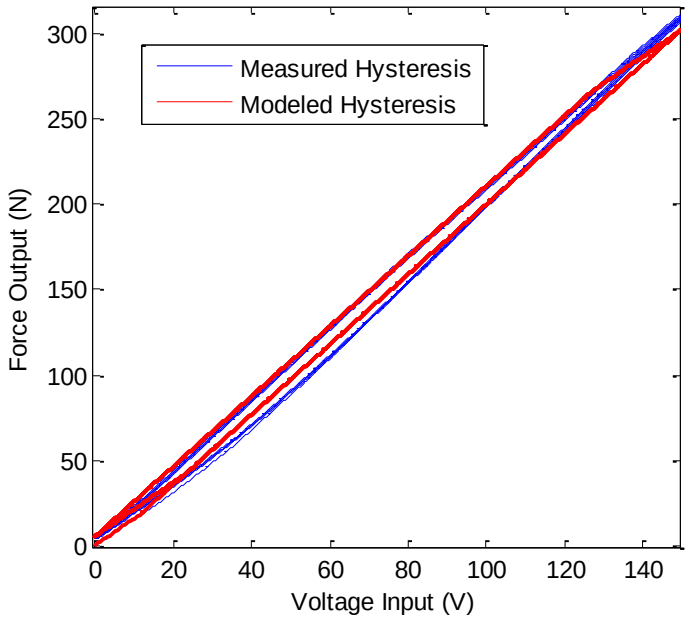

Figure 6.6. *Comparison between the measured (in blue) and the modeled hysteresis (in red) using the first set of data.*

The parameters of the direct and the inverse hysteresis models calculated through this method have been included in Table 6.1 and Table 6.2.

It was also mentioned in Section 3.1.1 that typically the most important changes occur in the region of the first few operators, meaning that out of that region the effect of the operators may even be negligible. This can be observed in these last two tables, where several weights for both the backlash and the one-sided dead zone operators are much smaller than the first few ones. Given these values, only the first two backlash operators and the first one-sided dead zone operators will be used and the rest will be omitted. Using only the first one-sided dead zone operator means that the whole block destined to account for the asymmetry will be nothing but a proportional gain given by its corresponding weight, considering that its dead zone is zero and therefore its output is equal to the input.

Table 6.1. *Parameters of the direct PI hysteresis model calculated with the first set of data.*

i	$\mathbf{r_i}$	$\mathbf{w_{hi}}$	**j**	$\mathbf{d_j}$	$\mathbf{w_{sj}}$
0	0	0,7824	0	0	0,4032
1	0,5769	0,2357	1	3,8634	$-1{,}3005\cdot10^{-10}$
2	1,1538	$4{,}2432\cdot10^{-8}$	-	-	-
3	1,7307	$1{,}0198\cdot10^{-8}$	-	-	-
4	2,3076	$3{,}3027\cdot10^{-9}$	-	-	-
5	2,8846	$1{,}6362\cdot10^{-9}$	-	-	-
6	3,4615	$1{,}1712\cdot10^{-9}$	-	-	-
7	4,0384	$1{,}1843\cdot10^{-9}$	-	-	-
8	4,6153	$1{,}4435\cdot10^{-9}$	-	-	-
9	5,1923	$1{,}8890\cdot10^{-9}$	-	-	-
10	5,7692	$2{,}5667\cdot10^{-9}$	-	-	-
11	6,3461	$3{,}6266\cdot10^{-9}$	-	-	-
12	6,923	$5{,}8633\cdot10^{-9}$	-	-	-

Table 6.2. *Parameters of the inverse PI hysteresis model calculated with the first set of data.*

i	$\mathbf{r'_i}$	$\mathbf{w'_{hi}}$	**j**	$\mathbf{d'_j}$	$\mathbf{w'_{sj}}$
0	0	1,278	0	0	2,4798
1	0,4513	-0,2959	1	1,5579	$7{,}9978\cdot10^{-10}$
2	1,0387	$-4{,}0934\cdot10^{-8}$	-	-	-
3	1,6261	$-9{,}8386\cdot10^{-9}$	-	-	-
4	2,2135	$-3{,}1861\cdot10^{-9}$	-	-	-
5	2,8009	$-1{,}5785\cdot10^{-9}$	-	-	-
6	3,3883	$-1{,}1298\cdot10^{-9}$	-	-	-
7	3,9756	$-1{,}1425\cdot10^{-9}$	-	-	-
8	4,5630	$-1{,}3925\cdot10^{-9}$	-	-	-
9	5,1504	$-1{,}8223\cdot10^{-9}$	-	-	-
10	5,7378	$-2{,}4761\cdot10^{-9}$	-	-	-
11	6,3461	$-3{,}4985\cdot10^{-9}$	-	-	-
12	6,923	$-5{,}6563\cdot10^{-9}$	-	-	-

In an analogous manner, the identification for the second set of data was started with low order parameters $n = 2$ and $m = 1$, and the parameter ε was set to be 0.01. After a number of iterations, a model with $n = 12$ and $m = 1$ was found to be accurate enough to the measured model, as observed in Figure 6.7. This second model differs the most from the measured hysteresis in two regions: the loading curve, and at high inputs. Nonetheless, out of said regions the model seems reasonably similar to the measured hysteresis. Again, it can be seen that the contribution of the one-sided dead zone operators is almost non-existent.

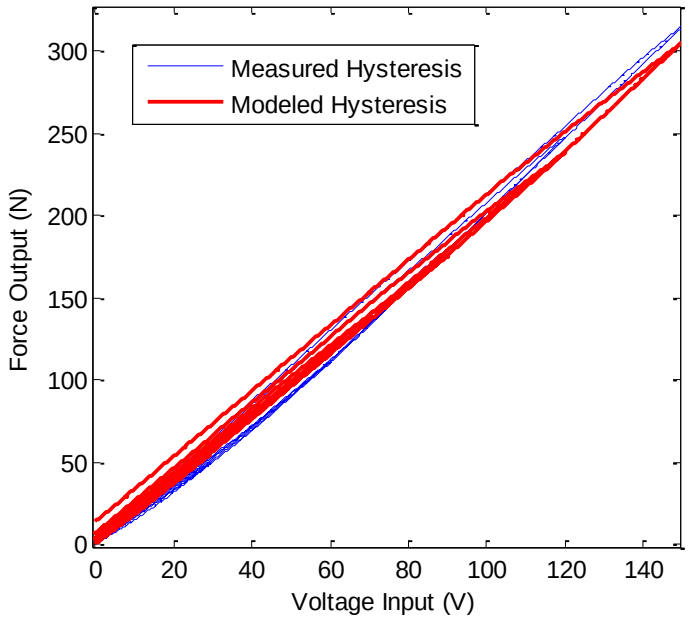

Figure 6.7. *Comparison between the measured (in blue) and the modeled hysteresis (in red) with the second set of data.*

The parameters of the direct and the inverse hysteresis models calculated through this method have been included in Table 6.3 and Table 6.4.

As it happened with the modeled firstly developed, not all the backlash and one-sided dead zone operators contribute equally to the direct and inverse models. Thus, the only backlash operators used for the model will be the ones with the indexes 0, 1, 2, 8 and 10, while the first one-sided dead zone operator is the only one considered significant. Again, since the first one-sided dead zone operator is the only one used and the block will be reduced to a proportional gain given by its corresponding weight.

Table 6.3. *Parameters of the direct PI hysteresis model calculated with the second set of data.*

i	$\mathbf{r_i}$	$\mathbf{w_{hi}}$	**j**	$\mathbf{d_j}$	$\mathbf{w_{sj}}$
0	0	0,8788	0	0	0,4066
1	0,5769	0,0441	1	3,8680	$-8{,}709\cdot10^{-13}$
2	1,1538	0,0551	-	-	-
3	1,7307	$1{,}7185\cdot10^{-11}$	-	-	-
4	2,3076	$7{,}4700\cdot10^{-12}$	-	-	-
5	2,8846	$9{,}7188\cdot10^{-12}$	-	-	-
6	3,4615	$1{,}2341\cdot10^{-11}$	-	-	-
7	4,0384	$2{,}6381\cdot10^{-11}$	-	-	-
8	4,6153	0,0465	-	-	-
9	5,1923	$3{,}893\cdot10^{-11}$	-	-	-
10	5,7692	0,0689	-	-	-
11	6,3461	$3{,}3843\cdot10^{-9}$	-	-	-
12	6,9230	$1{,}7939\cdot10^{-10}$	-	-	-

Table 6.4. *Parameters of the direct PI hysteresis model calculated with the second set of data.*

i	$\mathbf{r'_i}$	$\mathbf{w'_{hi}}$	**j**	$\mathbf{d'_j}$	$\mathbf{w'_{sj}}$
0	0	1,1379	0	0	2,4592
1	0,507	-0,0543	1	1,5728	$5{,}2672\cdot10^{-12}$
2	1,0394	-0,0611	-	-	-
3	1,6037	$-1{,}7964\cdot10^{-11}$	-	-	-
4	2,1679	$-7{,}8087\cdot10^{-12}$	-	-	-
5	2,7322	$-1{,}0159\cdot10^{-11}$	-	-	-
6	3,2965	$-1{,}29\cdot10^{-11}$	-	-	-
7	3,8608	$-2{,}7577\cdot10^{-11}$	-	-	-
8	4,4250	-0,0464	-	-	-
9	5,0162	$-3{,}7081\cdot10^{-11}$	-	-	-
10	5,6073	-0,0615	-	-	-
11	6,2382	$-2{,}8301\cdot10^{-9}$	-	-	-
12	6,8691	$-1{,}5001\cdot10^{-10}$	-	-	-

6.2.2. Results

The two inverse models calculated in the previous subchapter need to be tested in order to be able to decide which provides a better performance. Six different triangular periodic signals will be used as reference force inputs and the maximum hysteresis will be measured and later compared.

The results obtained when using the first of the two inverse models have been illustrated in Figure 6.8 to Figure 6.13, and the maximum hystereses calculated in each test have been gathered in Table 6.5.

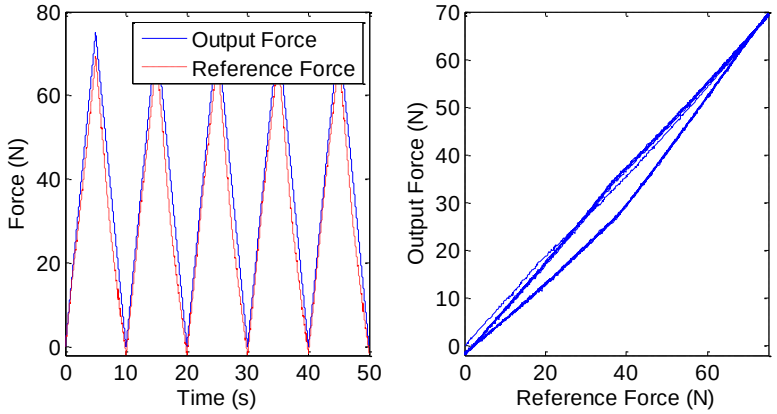

Figure 6.8. *Test No. 1, using a periodic triangular reference input with amplitude 75 N and frequency 0.1 Hz. Left, evolution of input and output. Right, hysteresis measured.*

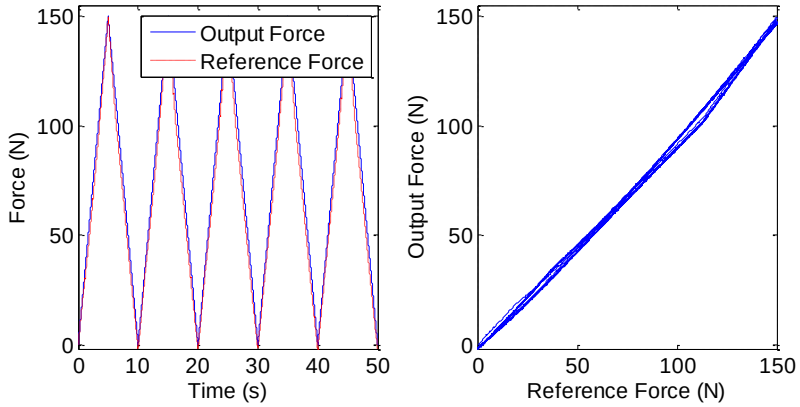

Figure 6.9. *Test No. 2, using a periodic triangular reference input with amplitude 150 N and frequency 0.1 Hz. Left, evolution of input and output. Right, hysteresis measured.*

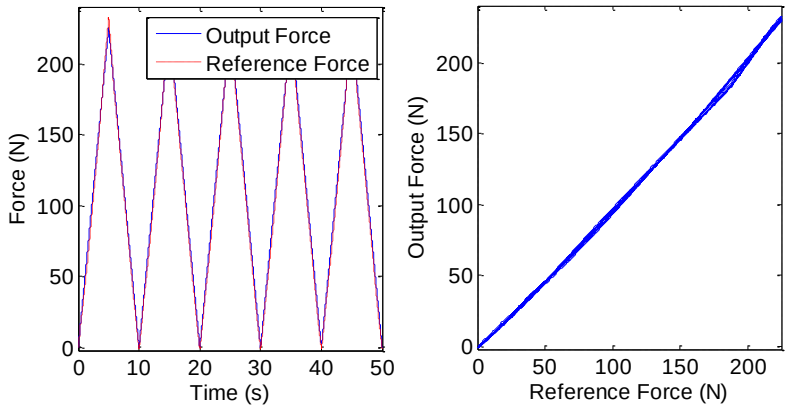

Figure 6.10. *Test No. 3, using a periodic triangular reference input with amplitude 225 N and frequency 0.1 Hz. Left, evolution of input and output. Right, hysteresis measured.*

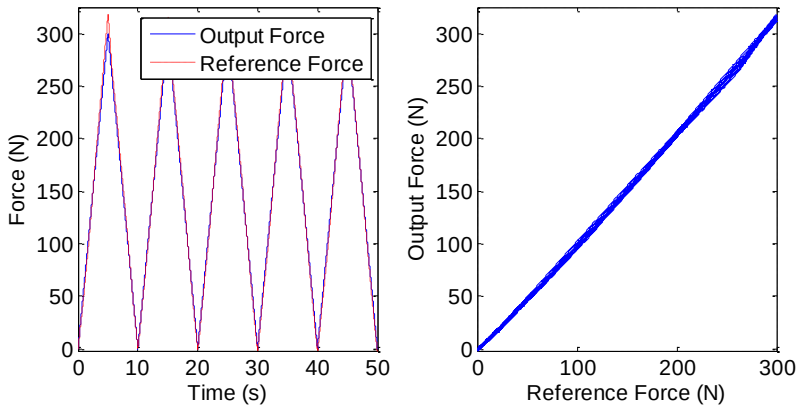

Figure 6.11. *Test No. 4, using a periodic triangular reference input with amplitude 300 N and frequency 0.1 Hz. Left, evolution of input and output. Right, hysteresis measured.*

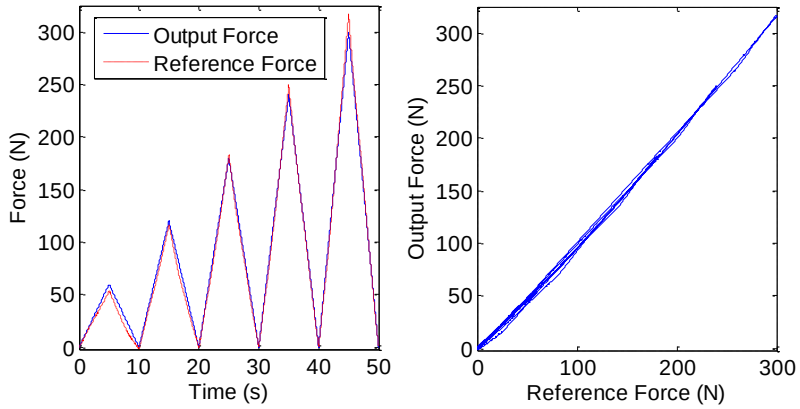

Figure 6.12. *Test No. 5, using a periodic triangular reference input with increasing amplitude and frequency 0.1 Hz. Left, evolution of input and output. Right, hysteresis measured.*

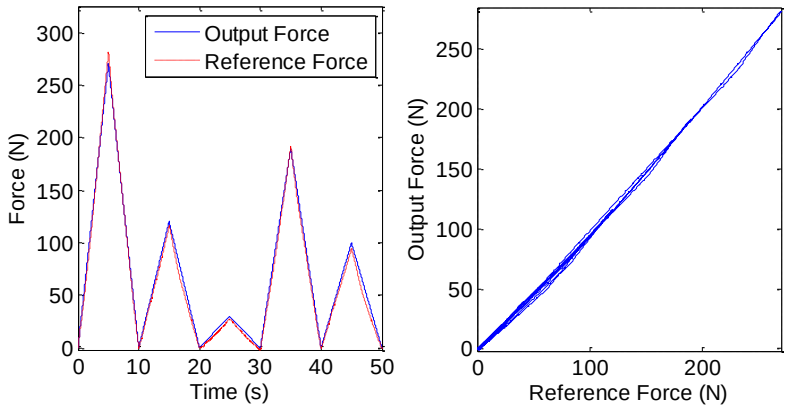

Figure 6.13. *Test No. 6, using a periodic triangular reference input with random amplitude and frequency 0.1 Hz. Left, evolution of input and output. Right, hysteresis measured.*

Table 6.5. *Maximum hysteresis measured when using different periodic triangular reference inputs.*

	Test No.					
	1	**2**	**3**	**4**	**5**	**6**
Max. Hysteresis (%)	11.9	3.64	2.21	2.67	3.56	3.28

The results obtained when using the second inverse model have been illustrated in Figure 6.14 to Figure 6.19, and the maximum hystereses calculated in each test have been gathered in Table 6.6.

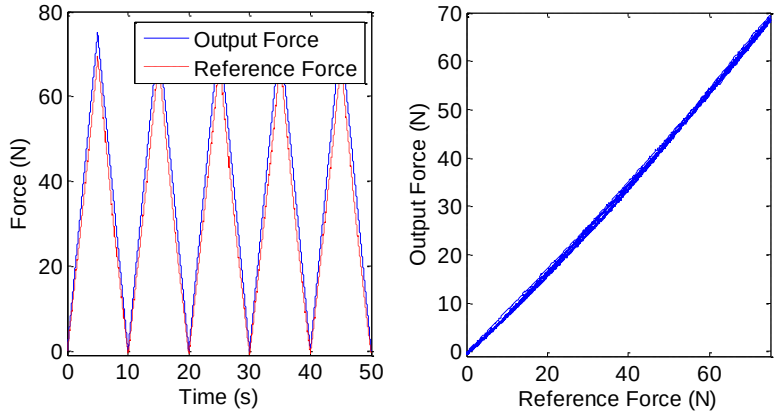

Figure 6.14. *Test No. 1, using a periodic triangular reference input with amplitude 75 N and frequency 0.1 Hz. Left, evolution of input and output. Right, hysteresis measured.*

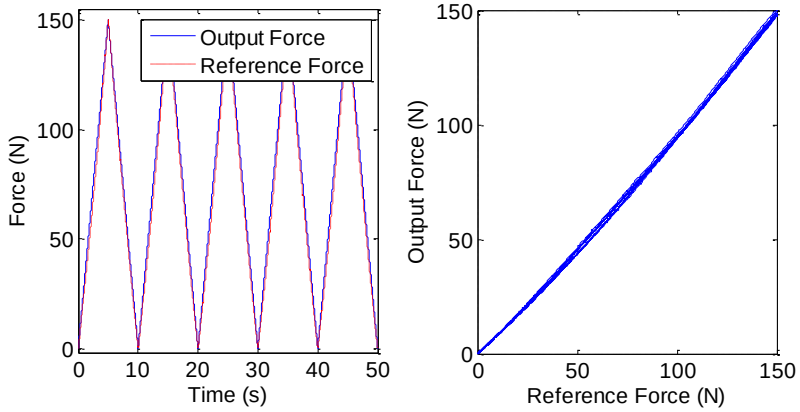

Figure 6.15. *Test No. 2, using a periodic triangular reference input with amplitude 150 N and frequency 0.1 Hz. Left, evolution of input and output. Right, hysteresis measured.*

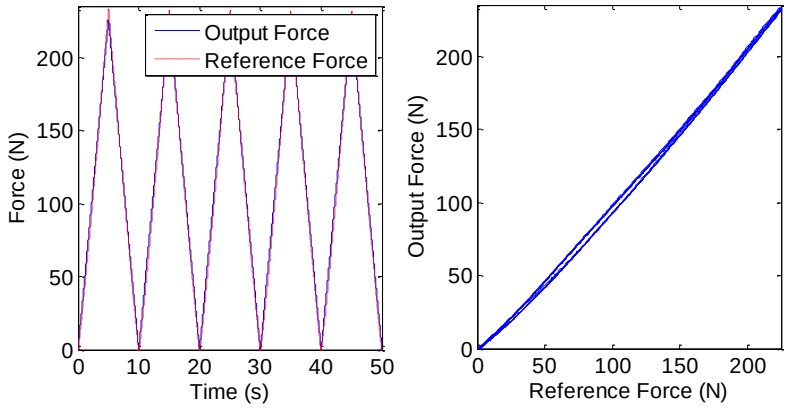

Figure 6.16. *Test No. 3, using a periodic triangular reference input with amplitude 225 N and frequency 0.1 Hz. Left, evolution of input and output. Right, hysteresis measured.*

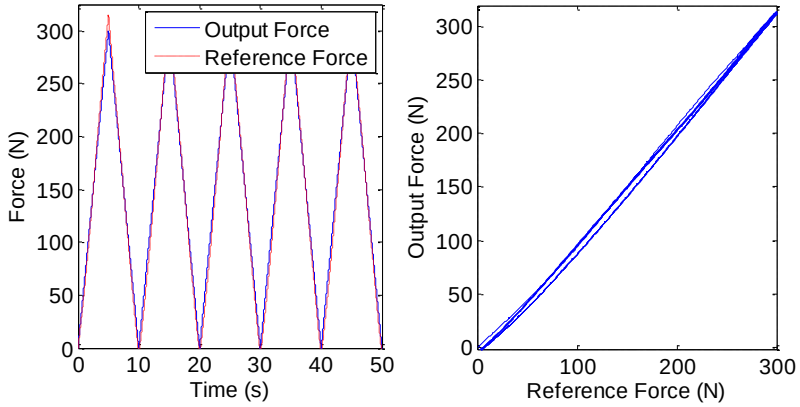

Figure 6.17. *Test No. 4, using a periodic triangular reference input with amplitude 300 N and frequency 0.1 Hz. Left, evolution of input and output. Right, hysteresis measured.*

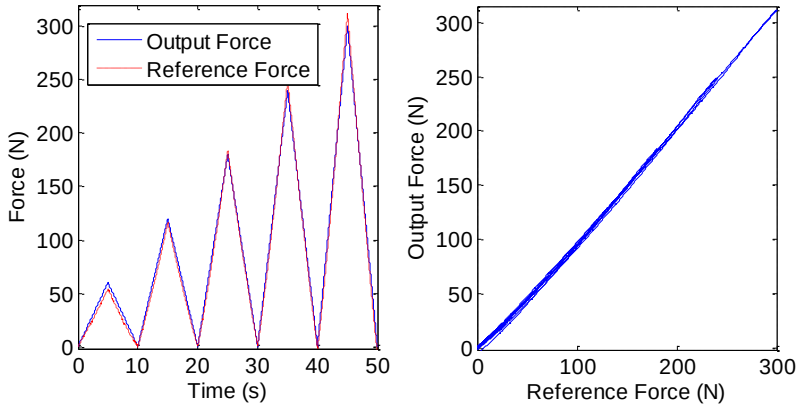

Figure 6.18. *Test No. 5, using a periodic triangular reference input with increasing amplitude and frequency 0.1 Hz. Left, evolution of input and output. Right, hysteresis measured.*

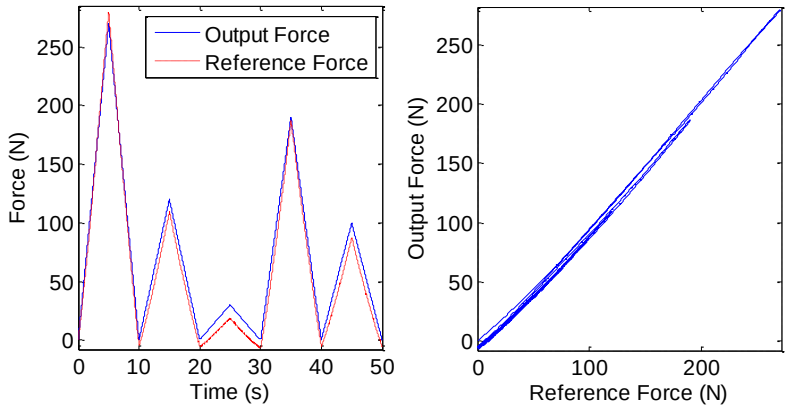

Figure 6.19. *Test No. 6, using a periodic triangular reference input with random amplitude and frequency 0.1 Hz. Left, evolution of input and output. Right, hysteresis measured.*

Table 6.6. *Maximum hysteresis measured when using different periodic triangular reference inputs.*

	Test No.					
	1	**2**	**3**	**4**	**5**	**6**
Max. Hysteresis (%)	1.55	1.33	2.03	2.74	1.85	2.99

When comparing the results with both models one can appreciate that the latter provides smaller maximum hysteresis in every test but test number 5, and even in that case the maximum hysteresis is barely higher. In conclusion, the second inverse model provides a better performance in the compensation of hysteresis and will therefore be utilized for the rest of the thesis work.

In addition, the results reveal that the gain is not constant, or in other words, that the relation between input and output is not entirely linear. This non-linearity may lead to a lack of performance and its effect will later be observed in the subsequent sections.

6.3. Creep Compensation

Creep or drift will be mitigated by calculating a model for said non-linearity and subsequently implementing it in an inverse multiplicative structure, as presented in Section 3.1.2. Even if the original creep was already measured to be considerably small (2.3 % after 120 s, as seen in Section 5.2) this compensation method was tested for a possible further improvement of the performance of the actuator.

Section 6.3.1 will be dedicated to the formulation of the creep model and the implementation of the inverse multiplicative structure to the system, whereas the performance of the compensation will be studied in Section 6.3.2.

6.3.1. Implementation

The technique proposed requires first to measure the creep of the system after the implementation of the hysteresis compensation. For this purpose, the step response with a reference input of 300 N over a period of 120 s, which can be seen in Figure 6.20, was measured and the creep was separated from it.

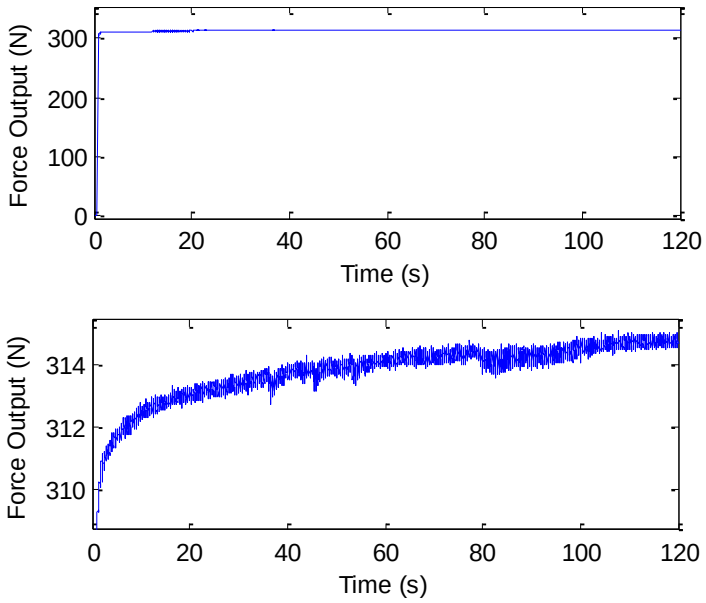

Figure 6.20. *Creep measured after the hysteresis compensation.*

Matlab and its system identification tool were used in order to identify the creep. The estimation from the original data was based on a process model, and several different models with different orders were tested. Starting with a low order process model, each time the simulation and the experimental result had to be compared and the order was increased if the match was not considered to be accurate enough. After some iterations, a model with three poles and one zero was found to be a good compromise between good resemblance between the simulated and experimental curves and low complexity. The identified model is:

$$C(s) = 0.0246 \cdot \frac{(1 + 29.074 \cdot s)}{(1 + 46.223 \cdot s) \cdot (1 + 1.5618 \cdot s) \cdot (1 + 0.001 \cdot s)} \tag{6.1}$$

Figure 6.21 displays the comparison between the measured and the modeled creep, proving the adequacy of the identified model.

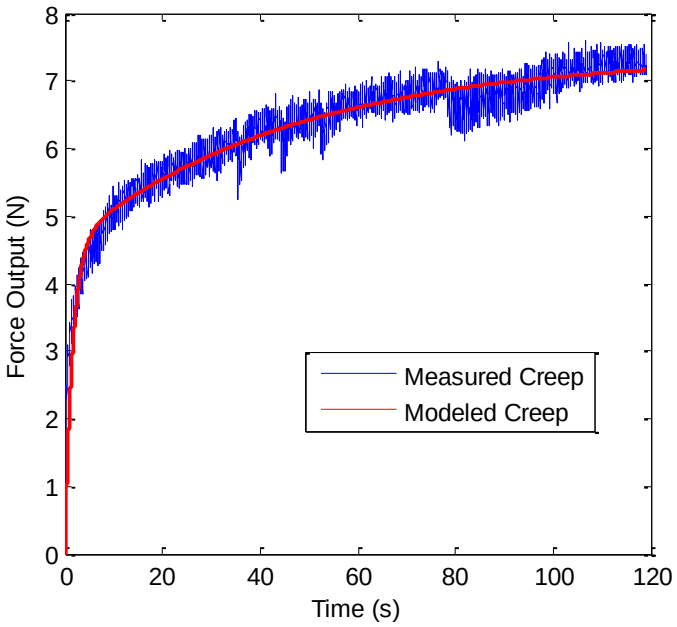

Figure 6.21. *Comparison between the measured (in blue) and modeled creep (in red).*

The other parameter that needs to be defined, the linear static gain K_c, was considered to be 1, assuming a good accuracy in the linearization accomplished by the hysteresis compensation.

6.3.2. Results

The creep compensation method was tested by implementing the inverse multiplicative structure to the system and using a step of 300 N as reference input. The result is shown in Figure 6.22.

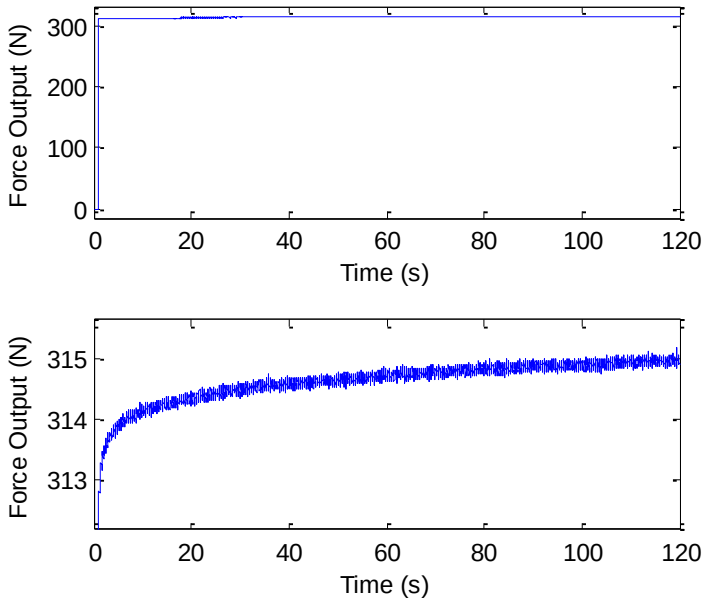

Figure 6.22. *Creep measured after implementing the hysteresis and creep compensations.*

After the compensation, creep was measured to be 0.96 %, an improvement when compared against the original value of 2.35 %. Thus, the creep compensation can be considered to be a success.

6.4. Vibration Compensation

This last compensation is essential in order to prevent higher forces being applied than the one desired, which may cause the actuator or the element being pressed to suffer damage or even break. The reference input will be transformed into a series of impulses with different amplitudes and delays by means of an input shaper in order to compensate the vibrations suffered in the system.

The parameters needed to define the input shaper will be calculated in Section 6.4.1, and the effectiveness of the compensation technique will be analyzed in Section 6.4.2.

6.4.1. Implementation

The calculation of the parameters of the input shaper first requires the identification of the oscillating step response of the system. In Section 5.3, dedicated to the characterization of the vibrations of the actuator, it was noted that for certain input values the output displayed a notch caused by an electromagnetic interference, leading to an important loss of information. After testing step inputs with different values, the response when using a reference force of 30 N was deemed to be the most appropriate given the absence of the aforementioned effect and that it provided clear enough

information on the oscillations of the system. The results of some of these tests have been included in Figure 6.23.

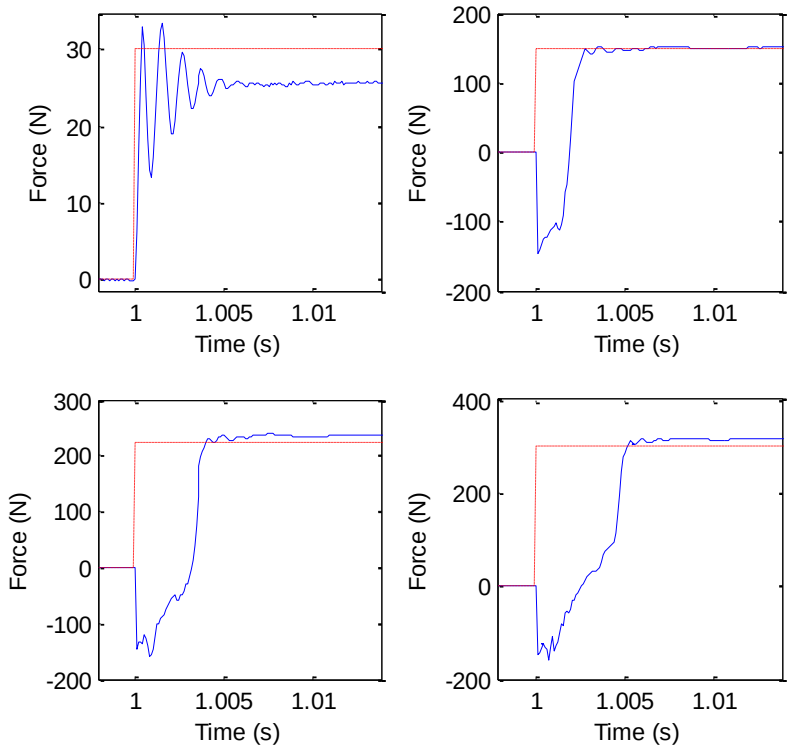

Figure 6.23. *Step responses (in blue) when using different reference force inputs (in red).*

The system identification tool from Matlab was again used for the model identification, basing the estimation on a process model. As mentioned in Section 3.1.3, it is recommended to model and identify the vibrations as the step response of a second order model system. Since this is but an approximation it is practically impossible to find a second order model that perfectly matches the experimental results. Therefore, the identification should focus on certain parameters that are deemed more important than others. In this case, it was found that the most crucial feature to be matched as closely as possible for a more effective compensation is the frequency. The model obtained with Matlab is shown and compared with the experimental result in Figure 6.24.

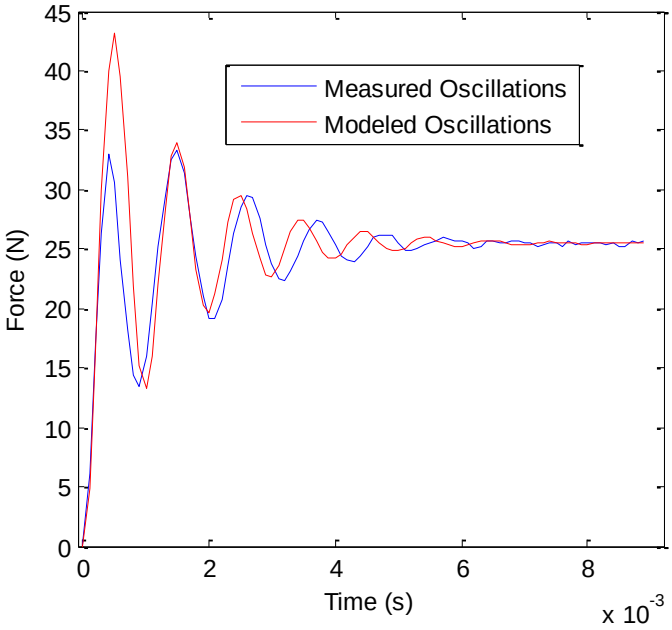

Figure 6.24. *Comparison between the measured (in blue) and the modeled oscillations (in red).*

And the identified model is:

$$V(s) = \frac{1}{2.441 \cdot 10^{-8} \cdot s^2 + 3.594 \cdot 10^{-5} \cdot s + 1} \tag{6.2}$$

From which the natural frequency and damping ratio can be inferred: $w_n = 6.44 \cdot 10^3\ rad/s, \xi = 0.115$.

These parameters will allow us to evaluate the amplitude and delay of each of the impulses created by the shaper. Several tests were carried out with different number of impulses, starting with a low number and increasing it by one each time until no improvement could be observed. In Figure 6.25 and Table 6.7 the results obtained with 2 to 5 impulses are depicted.

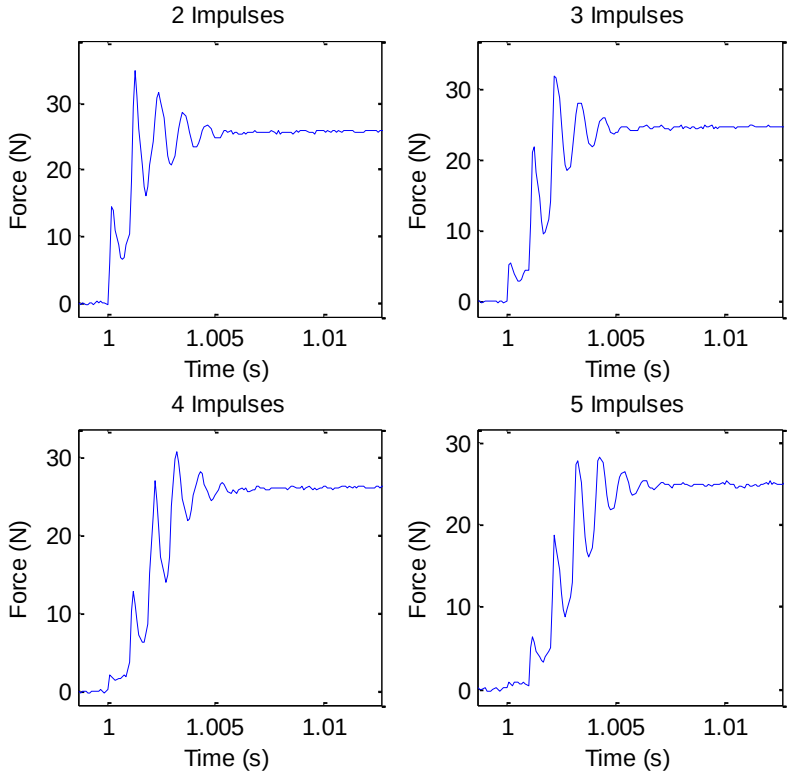

Figure 6.25. *Performance of the vibration compensation when using different numbers of impulses in the input shaper.*

Table 6.7. *Overshoot and settling time measured when using a different number of impulses in the input shaper.*

	Number of Impulses				
	1	**2**	**3**	**4**	**5**
Overshoot (%)	29.18	34.11	22.58	18.76	9.28
Settling Time (ms)	3.35	3.45	4	3.85	3.9

It was observed that using more than 5 impulses did not lead to any significant improvement either on the overshoot or the settling time. It should be noted that while a considerable reduction has taken place in the overshoot, which has been reduced to around one third of the original value, the settling time has however suffered an increase. Nevertheless, such increase can be considered to be negligible and the decrease in overshoot sufficient.

When using 5 impulses, the parameters defining the amplitude and delay of each impulse were calculated to be the ones included in Table 6.8, shown below.

Table 6.8. *Parameters of the input shaper for the vibration compensation.*

	Ith Impulse				
	1	**2**	**3**	**4**	**5**
A_i	0.0283	0.1627	0.3511	0.3368	0.1211
t_i (ms)	0	0.0982	2	2.9	3.9

6.4.2. Results

Since the identification was done based on the results when using a small reference force in order to prevent the effect of the electromagnetic interferences from causing a loss of information, the compensation should also be validated for higher inputs. Different levels of reference inputs were tested for this purpose, some of which can be seen in Figure 6.26. The overshoots and measuring times measured have been gathered in Table 6.9.

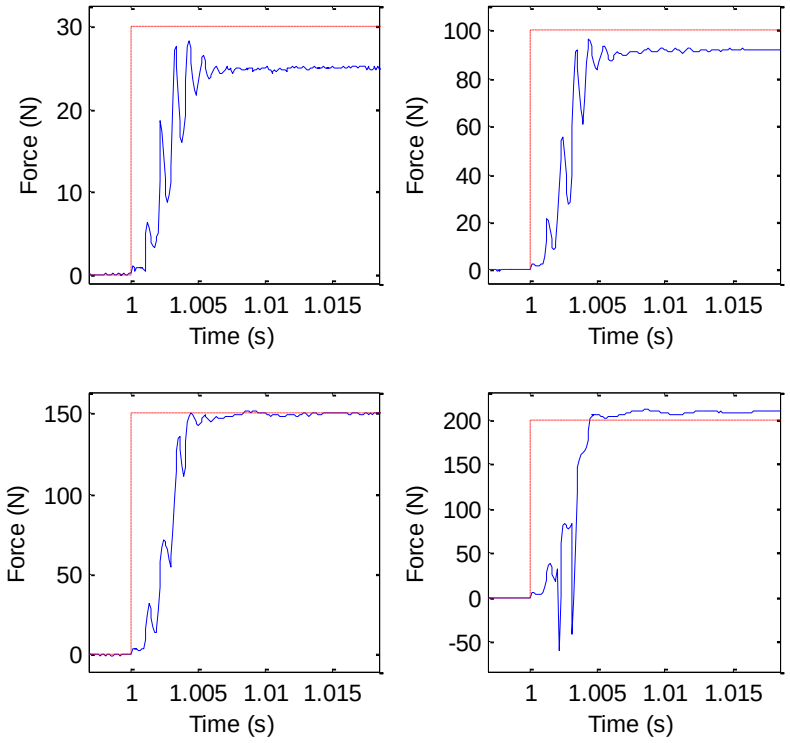

Figure 6.26. *Performance of the vibration compensation when using different reference force inputs.*

Table 6.9. *Overshoot and settling time when using different reference inputs.*

	Reference Force (N)			
	30	**100**	**150**	**200**
Overshoot (%)	9.28	4.76	0	0
Settling Time (ms)	3.9	4.05	4.05	4.25

These last results show that the vibration compensation is more effective when using higher inputs than the one it was designed for. Also, since the input is divided into different smaller impulses the effect of the electromagnetic interferences will now be present when using bigger inputs than before. To be more precise, in the last tests the anomalies were observed when using reference inputs around 200 N or bigger. The vibration compensation applied seemed to completely rid the step responses of overshoots when using higher inputs, but since some information was lost and the response was somehow distorted this could not be correctly verified.

Another important issue to be inferred from these results is the fact that the gain of the system is not constant, which was already taken into account in Section 6.2.2. The relation between the reference input and the output can be seen to vary in each test, which indicates the presence the aforementioned non-linearity that has not been taken care of.

6.5. Verification of the Control Methods

The three compensations implemented in the previous sections have been proven to be successful separately one after the other. However, it has yet to be studied if each of the last two compensations poses an obstacle to the one or ones previously applied. In order to do this some of the tests that have already been carried out in the previous sections will be repeated with the complete open-loop control.

First, the compensation for static hysteresis will be re-evaluated. Since the vibration compensation is intended for fast signals no negative effect was expected on the static hysteresis. The same six tests realized in Section 6.2.1 have been repeated and illustrated in Figure 6.27 to Figure 6.32, while the maximum hystereses have been collected in Table 6.10.

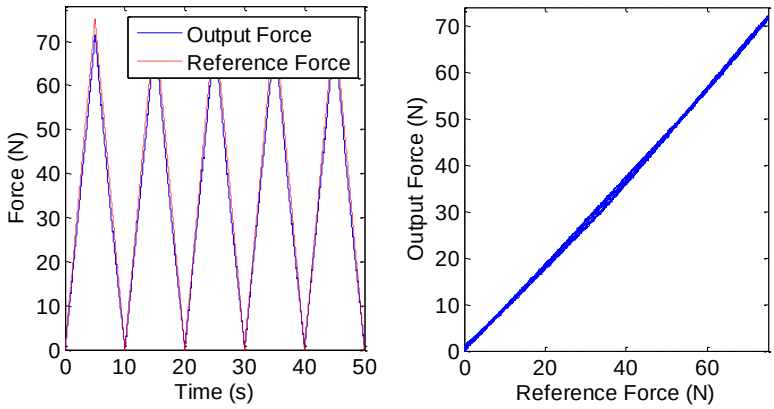

Figure 6.27. *Test No. 1, using a periodic triangular reference input with amplitude 75 N and frequency 0.1 Hz. Left, evolution of input and output. Right, hysteresis measured.*

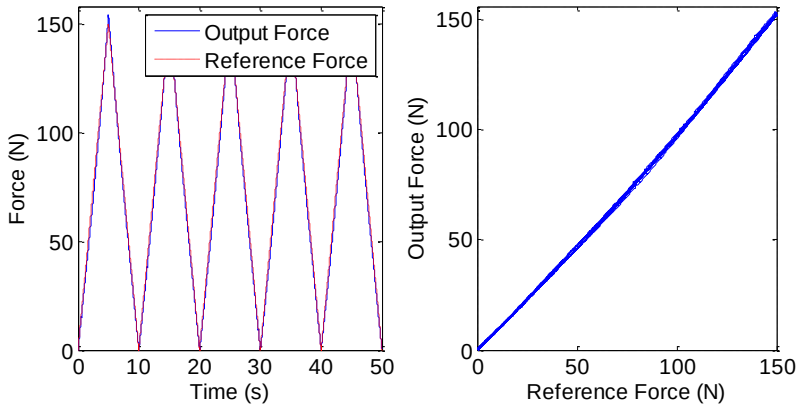

Figure 6.28. *Test No. 2, using a periodic triangular reference input with amplitude 150 N and frequency 0.1 Hz. Left, evolution of input and output. Right, hysteresis measured.*

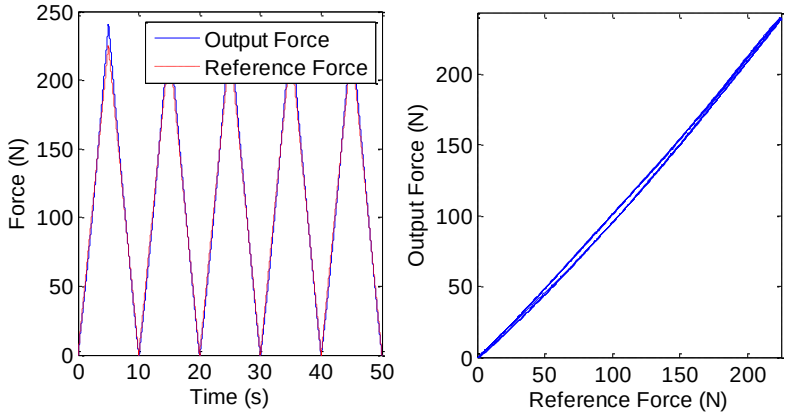

Figure 6.29. *Test No. 3, using a periodic triangular reference input with amplitude 225 N and frequency 0.1 Hz. Left, evolution of input and output. Right, hysteresis measured.*

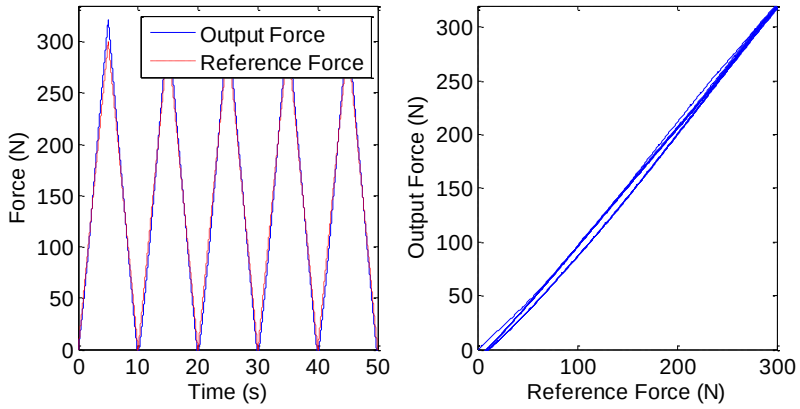

Figure 6.30. *Test No. 4, using a periodic triangular reference input with amplitude 300 N and frequency 0.1 Hz. Left, evolution of input and output. Right, hysteresis measured.*

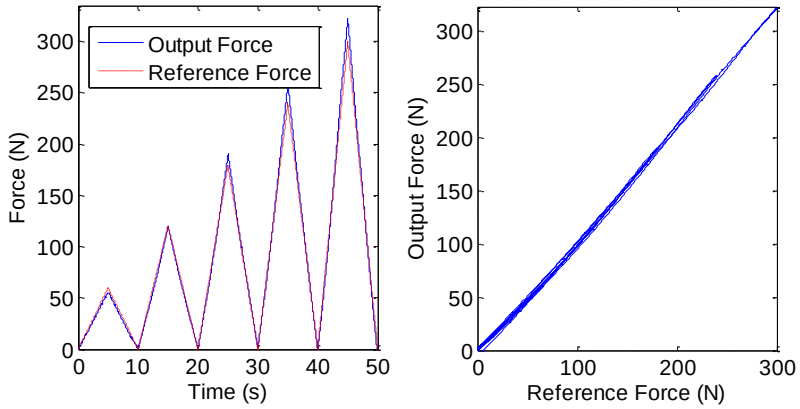

Figure 6.31. *Test No. 5, using a periodic triangular reference input with increasing amplitude and frequency 0.1 Hz. Left, evolution of input and output. Right, hysteresis measured.*

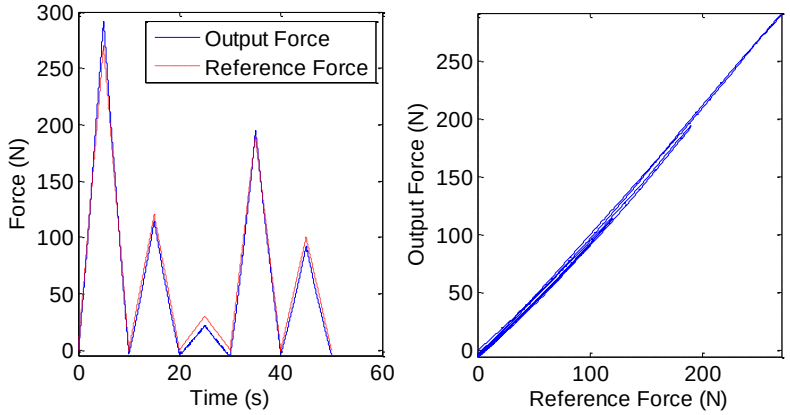

Figure 6.32. *Test No. 6, using a periodic triangular reference input with random amplitude and frequency 0.1 Hz. Left, evolution of input and output. Right, hysteresis measured.*

Table 6.10. *Maximum hysteresis measured when using different periodic triangular reference inputs.*

	Test Nº					
	1	**2**	**3**	**4**	**5**	**6**
Max. Hysteresis (%)	1.75	0.89	2.29	3.09	1.09	2.81

These results prove that, as suspected, the inclusion of the input shaper has no negative effect on the static hysteresis compensation. However, the working principle of the vibration compensation hints that it may affect the performance when using high frequencies. Dynamic hysteresis was thereby tested by using signals with different frequencies, and the results are shown in Figure 6.33 and Table 6.11.

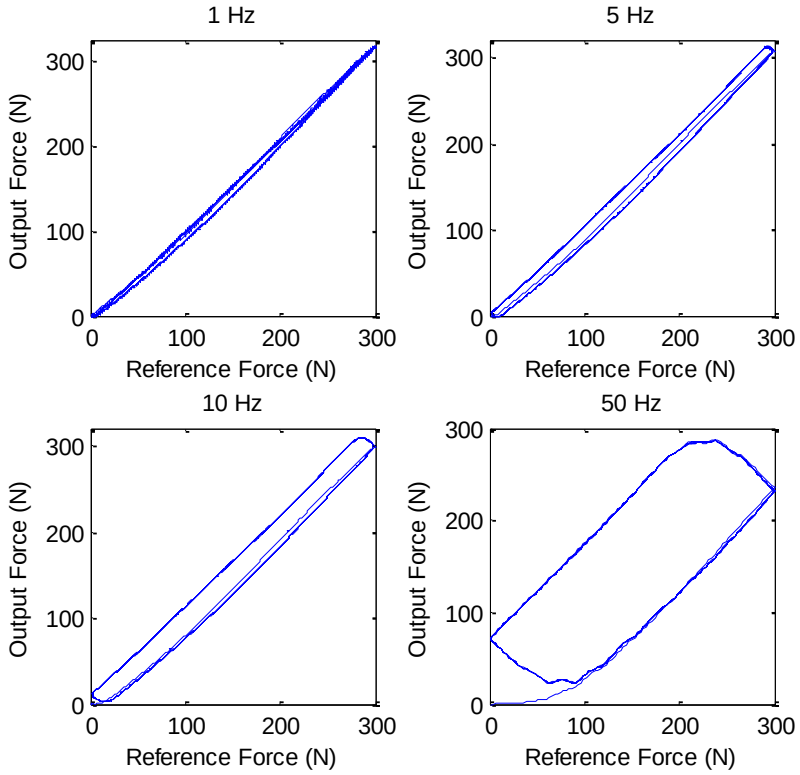

Figure 6.33. *Hysteresis curves when using a triangular periodic input with the maximum amplitude recommended and frequencies ranging from 1 to 50 Hz.*

Table 6.11. *Maximum hystereses calculated when using a triangular periodic input with the maximum amplitude recommended and frequencies ranging from 0.1 to 50 Hz.*

	Frequency (Hz)				
	0.1	**1**	**5**	**10**	**50**
Max. Hysteresis (%)	3.09	3.84	8.02	12.98	59.95

These results show that increasing the frequency of the input leads to a more notable deterioration in the hysteretic behavior than when applying no control at all, which can be seen in Figure 5.2 and Table 5.1. To definitely prove that this deterioration is due to

the vibration compensation the tests were repeated after removing the input shaper. The new results can be found in Figure 6.34 and Table 6.12.

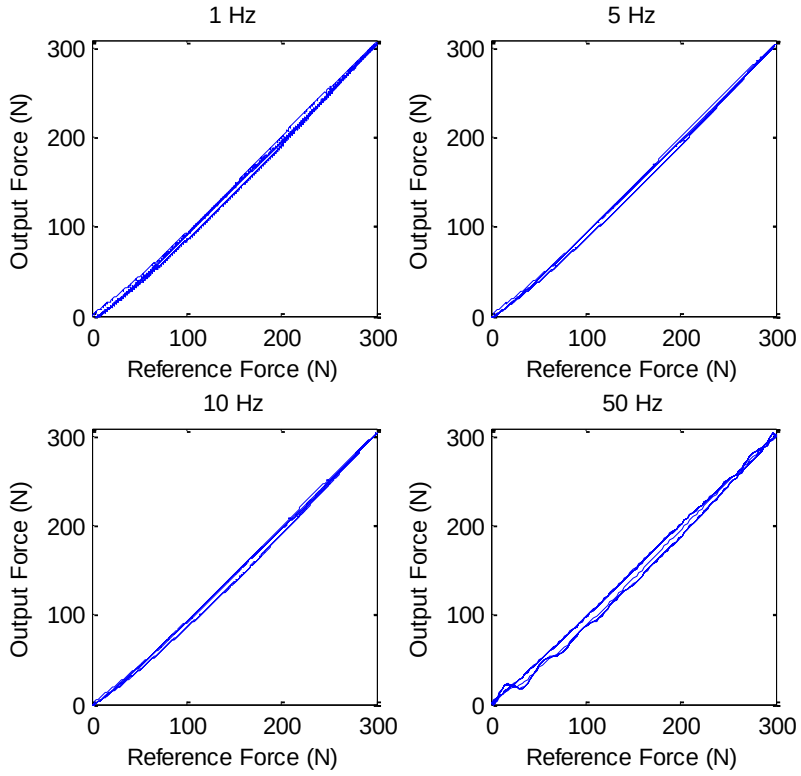

Figure 6.34. *Hysteresis curves when using a triangular periodic input with the maximum amplitude recommended and frequencies ranging from 1 to 50 Hz.*

Table 6.12. *Maximum hystereses calculated when using a triangular periodic input with the maximum amplitude recommended and frequencies ranging from 0.1 to 50 Hz.*

	Frequency (Hz)				
	0.1	**1**	**5**	**10**	**50**
Max. Hysteresis (%)	3.02	2.59	3.08	3.23	5.51

It can be seen from the maximum hystereses in Table 6.12 that the degradation when increasing the frequency is less pronounced now. Not only that, but also how the static hysteresis compensation can still be appreciated at different frequencies.

Even if the control was not supposed to deal with dynamic hysteresis given that the applications to which the actuator is destined do not require working at high frequencies, this helps propose that in spite of having a rate-dependant hysteresis compensator the input shaper might render it useless if combined. This hypothesis requires further study and will not be proven true or false in this thesis work.

The last test to verify the complete control is the measurement of the creep. Again, no negative effect is to be expected from the inclusion of the vibration compensation.

The creep measured in the step response when using a reference input force of 300 N after 120 s can be seen in Figure 6.35.

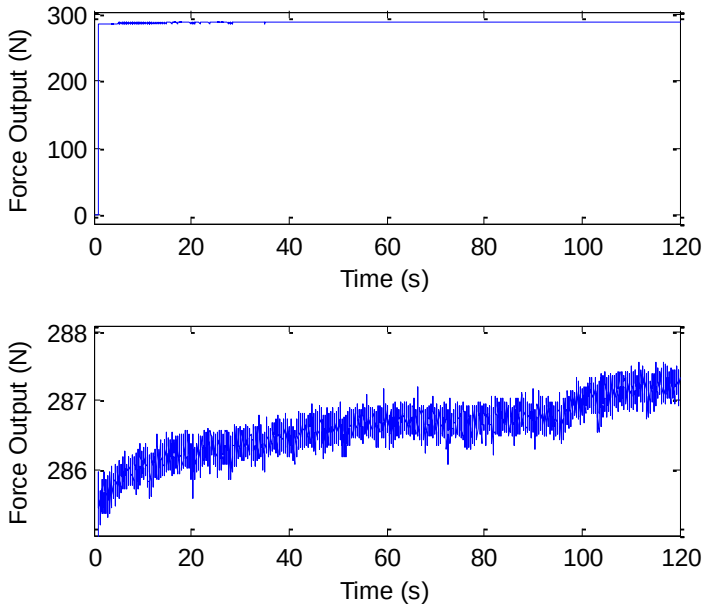

Figure 6.35. *Step response after 120 s (top) and detail of the creep measured from it (bottom).*

The creep was measured to be 0.63 %, which certifies that the vibration compensation does not interfere at all with the creep compensation as expected.

6.6. Tracking Performance

Apart from the nonlinearities and the unwanted vibrations, there is another feature that needs to be analyzed in order to establish how accurate the open-loop control designed is. The tracking performance will indicate how well the output force matches the reference force input.

First, the response of the system against a specific reference input was measured. The reference input selected consisted on a stair-like signal in which each step is reached after a 5 ms ramp, implies an increase of 10 N and lasts for 0.5 s. Several tests proved that using a ramp time of 5 ms leads to the total absence of overshoot and electromagnetic interferences in the measurements no matter what the value of the step was. This signal pretends to emulate the real working order of the actuator, using a number of fast steps to reach the desired output value.

Figure 6.36 depicts the output force in relation to the designed reference input force.

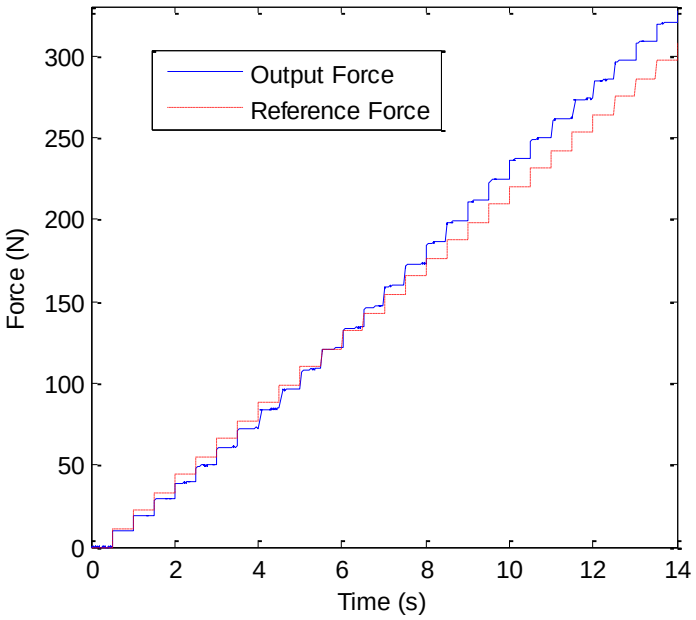

Figure 6.36. *Evolution of output and reference forces.*

The data collected thanks to the last measurement will allow us to determine the absolute error and the relative error, parameters that will quantify the tracking performance after the open-loop control. Both errors have been represented in Figure 6.37.

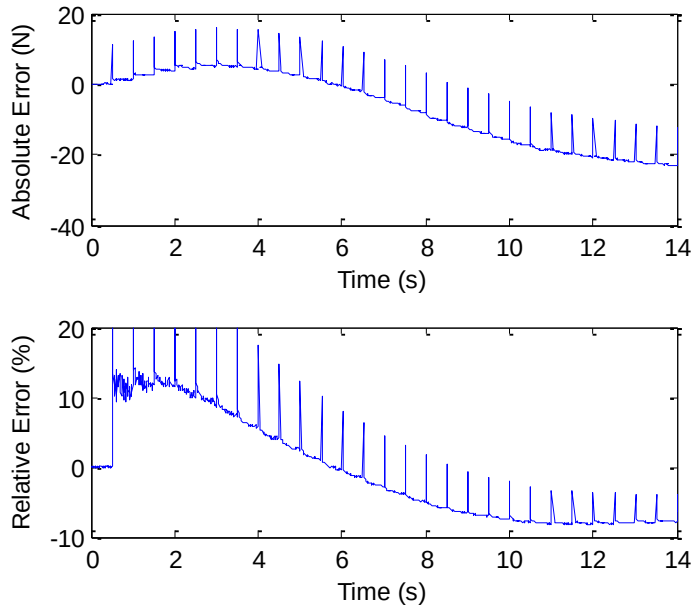

Figure 6.37. *Absolute error (top) and relative error (bottom).*

Ignoring the spikes present in both graphs, due to the difference between input and output during the delay suffered by the output, the maximum absolute error was calculated to vary from 5.37 N to -22.76 N, while the relative error varies from 12.08 %

to -8.08 %. It can be observed in the relative error that the extremes are found at low and high force values, precisely the same regions where the biggest discrepancies between the modeled and the measured hysteresis occur as seen in Figure 6.7 in a previous section of this chapter, which are also the same regions where gain suffers the biggest variations.

6.7. Conclusions

An open-loop controller based on three different compensation techniques has been successfully designed in this chapter: hysteresis compensation based on model inversion, creep compensation based on an inverse multiplicative structure and vibration compensation based on an input shaping technique. Static hysteresis, creep and vibrations have been reduced as shown in Table 6.13.

Table 6.13. *Hysteresis, creep and overshoot measured before and after implementing the open-loop control.*

	Uncontrolled	**Controlled**
Maximum Static Hysteresis	5.5 % - 6.17 %	1.55 % - 2.99 %
Creep	2.35 %	0.63 % - 0.96 %
Overshoot	25.92 %	0 % - 9.28 %

In addition, the tracking performance after the implementation of the control has been measured to be satisfactory, with a maximum relative error of 12.08 %.

However, even if the effectiveness of each compensation technique has been proven, some additional considerations are necessary for some of them.

First, the hysteresis model calculated through optimization in Section 6.2.1 is not a good fit to the real hysteresis curve at some ranges of values. The higher discrepancies occur at low and high input drives, precisely the same ranges of values where the higher tracking errors take place. A more precise model should lead to lower tracking errors and to an even more pronounced reduction of static hysteresis after the compensation.

Last, the vibration compensation technique proposed seems to pose an obstacle to rate-dependent hysteresis compensation, not considered however in this thesis work. Input shaping leads to a pronounced growth of the hysteresis curve when using high frequencies.

7. Conclusions

A force control scheme for a piezoelectric stack destined to force tests on paper fibers has been designed and implemented. The control involves the open-loop compensations of hysteresis, creep and vibrations, each of which have been individually achieved and later combined.

Some preliminary tasks had to be tackled before dealing with the control. The selection of the hardware needed for the experiments included the necessity to design a custom-built platform. This platform permits the attachment of the piezoelectric stack and manages an up-and-down movement thanks to a screw joined to a block by means of a ball bearing. Another essential point was the processing of the signal provided by the sensor used. An instrumentation amplifier was used for the amplification of the signal, whereas a low-pass filter and bypass capacitors were in charge of the filtering.

The hysteretic non-linearity was first compensated. A modified approach to the Prandtl-Ishlinskii method for modeling static hysteresis was used in order to account for possible asymmetries. This variation of the original method provided an inverse model that is both relatively accurate and easy to implement. The hysteresis compensation designed led to a reduction of the maximum static hysteresis measured in different experiments with diverse inputs from 6.17 % to 2.99 %.

Creep reduction was faced after hysteresis compensation. The creep compensator required modeling the creep non-linearity and adding it to an inverse multiplicative structure, thanks to which no model inversion is required. This compensator is implemented in cascade with the hysteresis compensator and the actuator. A reduction of the creep-nonlinearity was achieved from 2.35 % to less than 1 %.

The last phenomenon to be analyzed and compensated was the vibrations of the hysteresis and creep compensated system. An input shaper was designed based on the Zero Vibration or ZV input shaping technique, which divided the input into several impulses with different amplitudes and delays. Thus, each impulse could compensate the oscillations of the others and vice versa. The design of the input shaper was based on the oscillations observed at low input magnitudes, since the presence of electromagnetic interferences between the actuator and the sensor prevented measurements at higher input magnitudes from being correctly done. An input shaper with 5 impulses was selected, which lead to the reduction of the overshoot from 25.92 % at low input magnitudes to 9.28 % at low input magnitudes and the apparent complete removal of all oscillations at higher input magnitudes. A solution to the electromagnetic interferes should be proposed, which would lead to the complete characterization of the vibrations of the system and, therefore, to a better compensation.

The performance of the complete control scheme revealed however two main issues to be taken into consideration. On one hand, the implementation of the input shaper leads to a considerably pronounced growth of the dynamic hysteresis when increasing the frequency of the input. The combination of the input shaper along with a rate-dependent hysteresis compensator, if needed for any other application, should be examined in order to test if the input shaper renders the dynamic hysteresis compensator useless. On the other hand, the effect of the inaccuracies of the hysteresis model calculated can be observed in the variations suffered by the gain for different input values and in the tracking performance of the actuator after the implementation of the control. Such inaccuracies take place at low and high reference inputs, the same regions where the higher tracking errors occur. Two alternatives should be considered in future studies on this topic: on one hand, an alternative and more precise modeling method for the hysteresis; on the other, a non-linear input shaping method along with the initially proposed hysteresis model might compensate the changes suffered by the gain for different input values and accomplish a better performance. Albeit the results obtained show that the relative error can be kept under 12.08 % at all times and can be therefore considered to be satisfactory enough.

Open-loop displacement control methods such as the ones discussed in [42] and [54] have been proven also feasible for open-loop force control, while also providing a good performance on accuracy, speed and overshoot. Open-loop controllers are of great interest for sensorless applications in the domain of micro and nanomanipulation, such as the one to which the actuator studied is destined. The open-loop method proposed should also be applicable to actuators based on other working principles as long as certain conditions are met, a subject of interest for possible future studies. In addition, further research should focus on studying the robustness of the controller against certain parameter variations, internal or external to the system.

References

[1] Aburatani, H. A Piezoelectric Gripper Combined with a Smooth Impact Drive Mechanism. Proceedings of the Sixteenth International Symposium on Applications of Ferroelectrics (ISAF), Nara, Japan, May 27-31, 2007, pp. 779-782.

[2] Ahmad, M.A., Ismail, R., Ramli, M.S., Zawawi, M.A., Hambali, N., Abd Ghani, N.M. Vibration Control of Flexible Joint Manipulator Using Input Shaping with PD-Type Fuzzy Control Logic. Proceedings of the IEEE International Symposium on Industrial Electronics, Seoul, South Korea, July 5-8, 2009, pp. 1184-1189.

[3] Ang, W.T., Alija Garmón, F., Khosla, P., Riviere, C.N. Modeling Rate-Dependent Hysteresis in Piezoelectric Actuator. Proceedings of the 2003 IEEE/RSJ International Conference on Intelligent Robots and Systems, Las Vegas, USA, October 27 – November 1, 2003, pp. 1975-1980.

[4] Arnau Vives, A. Piezoelectric Transducers and Applications. 2nd Edition. Germany 2008, Springer. 532 p.

[5] Badel, A., Qiu, J., Nakano, T. Self-Sensing Force Control of a Piezoelectric Actuator. IEEE Transactions on Ultrasonics, Ferroelectrics and Frequency Control, 55(2008)12, pp. 2571-2581.

[6] Brogan, J., Fortgang, J., Singhose, W. Experimental Verification of Vibration Absorbers Combined with Input Shaping for Oscillatory Systems. Proceedings of the 2003 American Control Conference, Denver, USA, 2003, pp. 3160-3165 (Vol. 4).

[7] Burr-Brown Corporation. INA118 Datasheet. USA 1998. 16 p.

[8] Croft, D., Shedd, G., Devasia, S. Creep, Hysteresis, and Vibration Control for Piezoactuators: Atomic Force Microscopy Application. Proceedings of the 2000 American Control Conference, Chicago, USA, June 28-30, 2000, pp. 2123-2128.

[9] Edeler, C., Fatikow, S. Open Loop Force Control of Piezo-Actuated Stick-Slip Drives. International Journal of Intelligent Mechatronics and Robotics, 1(2011)1, pp. 1-19.

[10] Eielsen, A.A., Fleming, A.J. Passive Shunt Damping of Piezoelectric Stack Nanopositioner. Proceedings of the American Control Conference (ACC), Baltimore, USA, June 30 - July 2, 2010, pp. 4963-4968.

[11] Eisinberg, A., Menciassi, A., Micera, S., Campolo, D., Carrozza, M.C., Dario, P. PI Force Control of a Microgripper for Assembling Biomedical Microdevices. IEEE Proceedings – Circuits, Devices and Systems 148(2001)6, pp. 348-352.

[12] Fortgang, J., Singhose, W. Concurrent Design of Input Shaping and Vibration Absorbers. Proceedings of the 2002 American Control Conference, Alaska, USA, May 8-12, 2002, pp. 1491-1496 (Vol. 2).

[13] Giraud, F., Semail, B., Audren, J.-T. Analysis and Phase Control of a Piezoelectric Travelling-Wave Ultrasonic Motor for Haptic Stick Application. IEEE Transactions on Industry Applications 40(2004)6, pp. 1541-1549.

[14] Hagood, N.W., McFarland, A.J. Modeling of a Piezoelectric Rotary Ultrasonic Motor. IEEE Transactions on Ultrasonics, Ferroelectrics and Frequency Control 42(1995)2, pp. 210-224.

[15] Hongxia, J., Wanli, L., Singhose, W. Using Two-Mode Input Shaping to Repress the Residual Vibration of Cherry Pickers. Proceedings of the Third International Conference on Measuring Technology and Mechatronics Automation, Shanghai, China, January 6-7, 2011, pp. 1091-1094.

[16] Huang, X., Cai, J., Wang, M., Lv, X. A Piezoelectric Bimorph Micro-Gripper with Micro-Force Sensing. Proceedings of the IEEE International Conference on Information Acquisition, Hong Kong, China, June 27 – July 3, 2005, pp. 145-149.

[17] Isotech. DC Power Supply Alimentation C.C. England. 24 p.

[18] Itoh, T., Kobayashi, T., Okada, H., Masuda, T., Suga, T. A Digital Output Piezoelectric Accelerometer for Ultra-Low Power Wireless Sensor Node. Proceedings of the IEEE Conference on Sensors, Lecce, Italy, October 26-29, 2008, pp. 542-545.

[19] Janocha, H., Kuhnen, K. Real-Time Compensation of Hysteresis and Creep in Piezoelectric Actuators. Sensors and Actuators A: Physical, 79(2000)2, pp. 83-89.

[20] Jie, G., Xiangdong, L., Xiaozhong, L., Li, L. Dynamic Preisach Model and Inverse Compensation for Hysteresis of Piezoceramic Actuator based on Neural Networks. Proceedings of the 29th Chinese Control Conference, Beijing, China, July 29-31, 2010, pp. 446-451.

[21] Kallio, P., Kuncová-Kallio, J., Savia, M., Zhou, Q. ACI-51006 Introduction to Microsystem Technology. Tampere 2008, Tampere University of Technology. 173 p.

[22] Kappel, L., Hirn, U., Bauer, W., Schennach, R. A Novel Method for the Determination of Bonded Area of Individual Fiber-Fiber Bonds. Nordic Pulp and Paper Research Journal, 24(2009)2, pp. 199-205.

[23] Kazaryan, A.A. A Thin-Film Piezoelectric Pressure Sensor. Measurement Techniques, 45(2002)5, pp. 515-518.

[24] Kern, T.A. Engineering Haptic Devices: A Beginner's Guide for Engineers. 1st Edition. Germany 2009, Springer-Verlag and Heidelberg GmbH & Co. 504 p.

[25] Kuhnen, K., Janocha, H. Complex Hysteresis Modeling of a Broad Class of Hysteretic Actuator Nonlinearities. Proceedings of the 8th International Conference on New Actuators, Bremen, Germany, June 10-12, 2002, pp.688-691.

[26] Kunder, K.S. Power Supply Noise Reduction. Last updated 11.05.2006, 12 p. [accessed on 02.02.2012]. Available at: www.designers-guide.org/design.

[27] Li, Z., Aljanaideh, O., Su, C.-Y., Rakheja, S., Al Janaideh, M. Compensation of Hysteresis Nonlinearity for a Piezoelectric Actuator Using a Stop Operator-Based Prandtl-Ishlinskii Model. Proceedings of the 2011 International Conference on Advanced Mechatronic Systems, Zhengzhou, China, August 11-13, 2011, pp.169-174.

[28] Lim, C.K., He, S., Chen, I.-M., Yeo, S.H. A Piezo-On-Slider Type Linear Ultrasonic Motor for the Application of Positioning Stages. Proceedings of the IEEE/ASME International Conference on Advanced Intelligent Mechatronics, Atlanta, USA, September 19-23, 1999, pp. 103-108.

[29] Measurement Computing. PCI-DAS1001 Multifunction Analog & Digital I/O User's Guide. USA 2009. 24 p.

[30] Microelectronik GmbH. Precise Optical Measurements: Intelligent Sensors & Measuring-Systems. Germany 2012. 26 p.

[31] Minase, J., Lu, T.-F., Cazzolato, B., Grainger, S. Adaptative Identification of Hysteresis and Creep in Piezoelectric Stack Actuators. The International Journal of Advanced Manufacturing Technology 46(2010)9-12, pp. 913-921.

[32] Nader, J. Piezoelectric-Based Vibration Control: From Macro to Micro/Nano Scale Systems. 1st Edition. USA 2009, Springer New York. 517 p.

[33] Nguyen, Q.H., Han, Y.-M., Choi, S.-B., Hong, S.-M. Dynamic Characteristics of a New Jetting Dispenser Driven by Piezostack Actuator. IEEE Transactions on Electronics Packaging Manufacturing 31(2008)3, pp. 248-259.

[34] Omega Engineering, Inc. LC302/LCM302 Load Cell Series. In: Omega's Product Handbook, 2011, p.F-24.

[35] Oltronix Industrial Power Supplies b. v. Labpac Linear Power Supplies: B-Series. Netherlands 2007, Oltronix Industrial Power Supplies b. v. 4 p.

[36] Piezo Systems, Inc. Piezo Linear Amplifier. In: Piezo Systems, Inc. Catalog #8, Germany 2011, pp. 4-5.

[37] Piezomechanik GmbH. Piezo-Mechanical and Electrostrictive Stack and Ring Actuators: Product Range and Technical Data. 2004, Piezomechanik GmbH. 48 p.

[38] Pons, J.L. Emerging Actuator Technologies: A Micromechatronic Approach. 1st Edition. England 2005, Wiley. 304 p.

[39] Priya, S., Inman, D.J. Energy Harvesting Technologies. USA 2008, Springer-Verlag New York. 540 p.

[40] Rakotondrabe, M., Clévy, C., Lutz, P. Modelling and Robust Position/Force Control of a Piezoelectric Microgripper. Proceedings of the IEEE International Conference on Automation Science and Engineering, Scottsdale, USA, September 22-25, 2007, pp. 39-44.

[41] Rakotondrabe, M., Clévy, C., Lutz, P. Hysteresis and Vibration Compensation in a Nonlinear Unimorph Piezocantilever. Proceedings of the IEEE/RSJ International Conference on Intelligent Robots and Systems, Nice, France, September 22-26, 2008, pp. 558-563.

[42] Rakotondrabe, M., Clévy, C., Lutz, P. Complete Open Loop Control of Hysteretic, Creeped, and Oscillating Piezoelectric Cantilevers. IEEE Transactions on Automation Science and Engineering, 7(2010)3, pp. 440-450.

[43] Rakotondrabe, M., Haddab, Y., Lutz, P. Plurilinear Modeling and Discrete μ-Synthesis Control of a Hysteretic and Creeped Unimorph Piezoelectric Cantilever. Proceedings of the 9th International Conference on Control, Automation, Robotics and Vision, Singapore, December 5-8, 2006, pp. 1-8.

[44] Rakotondrabe, M., Haddab, Y., Lutz, P. Nonlinear Modeling and Estimation of Force in a Piezoelectric Cantilever. Proceedings of the 2007 IEEE/ASME International Conference on Advanced Intelligent Mechatronics, Zurich, Switzerland, September 4-7, 2007, pp. 1-6.

[45] Rakotondrabe, M., Haddab, Y., Lutz, P. Quadrilateral Modelling and Robust Control of a Nonlinear Piezoelectric Cantilever. IEEE Transactions on Control Systems Technology, 17(2009)3, pp. 528-539.

[46] Rakotondrabe, M., Le Gorrec, Y. Force Control in Piezoelectric Microactuators Using Self-Scheduled H_∞ Technique. Proceedings of the 5th IFAC Symposium on Mechatronic Systems, Massachusetts, USA, September 13-15, 2010, pp. 417-422.

[47] Reza Moheimani, S.O., Fleming, A. J. Piezoelectric Transducers for Vibration Control and Damping (Advances in Industrial Control). 1st Edition. Germany 2006, Springer Berlin. 287 p.

[48] Rong, W., Zhang, S., Liu, X., Yu, M. A Drive-Control System for 3D Piezoelectric Stick-Slip Positioner. Proceedings of the 6th International Forum on Strategic Technology, Harbin, China, August 22-24, 2011, pp. 317-322.

[49] Ronkanen, P., Kallio, P., Koivo, H.N. Simultaneous Actuation and Force Estimation Using Piezoelectric Actuators. Proceeding of the International Conference on Mechatronics and Automation, Harbin, China, August 5-8, 2007, pp. 3261-3265.

[50] Ronkanen, P. Current Measurement in Control and Monitoring of Piezoelectric Actuators. PhD Thesis. Tampere 2008. Tampere University of Technology. Publication - Tampere University of Technology. Publication 723. 134 p.

[51] Safari, A., Akdogan, E.K. Piezoelectric and Acoustic Materials for Transducer Applications. 1st Edition. USA 2008, Springer-Verlag New York. 481 p.

[52] Saketi, P., Kallio, P. Microrobotic Platform for Making, Manipulating and Breaking Individual Paper Fiber Bonds. Proceedings of the 2011 IEEE International Symposium on Assembly and Manufacturing, Tampere, Finland, May 25-27, 2011, pp. 1-6.

[53] Salvini, A., Fulginei, F.R., Pucacco, G. Generalization of the Static Preisach Model for Dynamic Hysteresis by a Genetic Approach. IEEE Transactions on Magnetics, 39(2003)3, pp. 1353-1356.

[54] Shen, J.-C., Chiang, H.-K., Shu, Y.-L. Precision Tracking Control of a Piezolectric-Actuated System. Proceedings of the Mediterranean Conference on Control and Automation, Athens, Greece, June 27-29, 2007, pp. 1-6.

[55] Shevtsov, V.K. Piezoelectric Sensor for High Sound Pressure Levels. Strength of Materials 4(1972)10, pp. 1249-1252.

[56] Simmers, G.E., Hodgkins, J.R., Mascarenas, D.D., Park, G., Sohn, H. Improved Piezoelectric Actuation. Journal of Intelligent Material Systems and Structures, 15(2004)12, pp. 941-953.

[57] Singhose, W., Derezinski, S., Singer, N. Extra-Insensitive Input Shapers for Controlling Flexible Spacecraft. Journal of Guidance, Control and Dynamics, 19(1996)2, pp. 385-391.

[58] SUP Bearing Co., Ltd. Mini-Thrust Ball Bearings Catalog. SUP Bearing Website [accessed on 28.11.2011]. Available at: http://www.supbearing.com.

[59] Tan, U.-X., Latt, W.T., Shee, C.Y., Riviere, C.N., Ang, W.T. Modeling and Control of Piezoelectric Actuators for Active Physiological Tremor Compensation. In: Nilanjan Sarkar (Ed.). Human-Robot Interaction. 1st Edition. Austria 2007, Itech Education and Publishing. 522 p.

[60] Tan, U.-X., Latt, W.T., Shee, C.Y., Riviere, C.N., Ang, W.T. Feedforward Controller of Ill-Conditioned Hysteresis Using Singularity-Free Prandtl-Ishlinskii Model. IEEE/ASME Transactions on Mechatronics, 14(2009)5, pp. 598-605.

[61] Tanikawa, T., Kawai, M., Koyachi, N., Arai, T., Ide, T., Kaneko, S., Ohta, R., Hirose, T. Force Control System for Autonomous Micro-Manipulation. Proceedings of the IEEE International Conference on Robotics and Automation, Seoul, South Korea, May 21-26, 2001, pp. 610-615 (Vol. 1).

[62] Topward Electric Instruments Co. Power Supplies Catalog. USA 2000. 4 p.

[63] Xu, Q., Wong, P.-K., Li, Y. Rate-Dependent Hysteresis Modeling and Compensation Using Least-Squares Support Vector Machines. Proceedings of the 8th International Conference on Advances in Neural Networks. Volume 2. Germany 2011, Springer-Verlag Berlin, pp. 85-93.

[64] Yang, H., Guo, H. Design of a Bulk-Micromachined Piezoelectric Accelerometer. IEEE Ultrasonics Symposium, New York, USA, October 28-31, 2007, pp. 2598-2601.

[65] Yuan, X., Qiu, J.-H., Ji, H.-L., Sun, J., Qiu, T. Design and Test of a Novel Piezoelectric Stack Pump. Proceedings of the Symposium on Piezoelectricity, Acoustic Waves and Device Applications , Xiamen, China, December 10-13, 2010, pp. 354-359.

[66] Yuasa Batteries, Inc. NP Series Data Sheet: NP7-12. USA 2008. 2 p.

[67] Zhang, Z., Hu, H. Design of a Novel Piezoelectric Inchworm Actuator. Proceedings of the International Conference on Electrical Machines and Systems, Wuhan, China, October 17-20, 2008, pp. 3707-3711.

[68] Zhao, F., García-Izaguirre, J., Martínez, J. Piezo-Stack Press. Tampere 2011, Tampere University of Technology. Student Report. 48 p.

Appendix A: Designs of the Test Platform

This appendix includes the plans with all the information needed on the different pieces comprising the structure of the test platform designed. The drawings are shown in the following pages in the following order:

- Base (1 pc.)
- Leg (2 pcs.)
- Actuator Bearer (1 pc.)
- Upper Platform (1 pc.)
- Supporting Rod (4 pcs.)

The drawings have been executed with SolidWorks. The dimensions of the measurements are in millimeters.

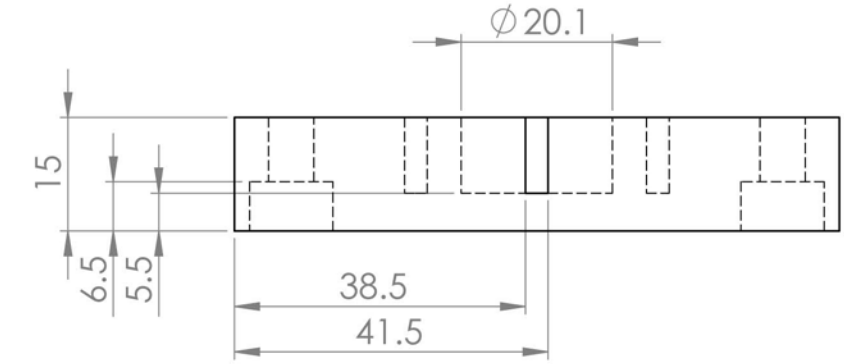

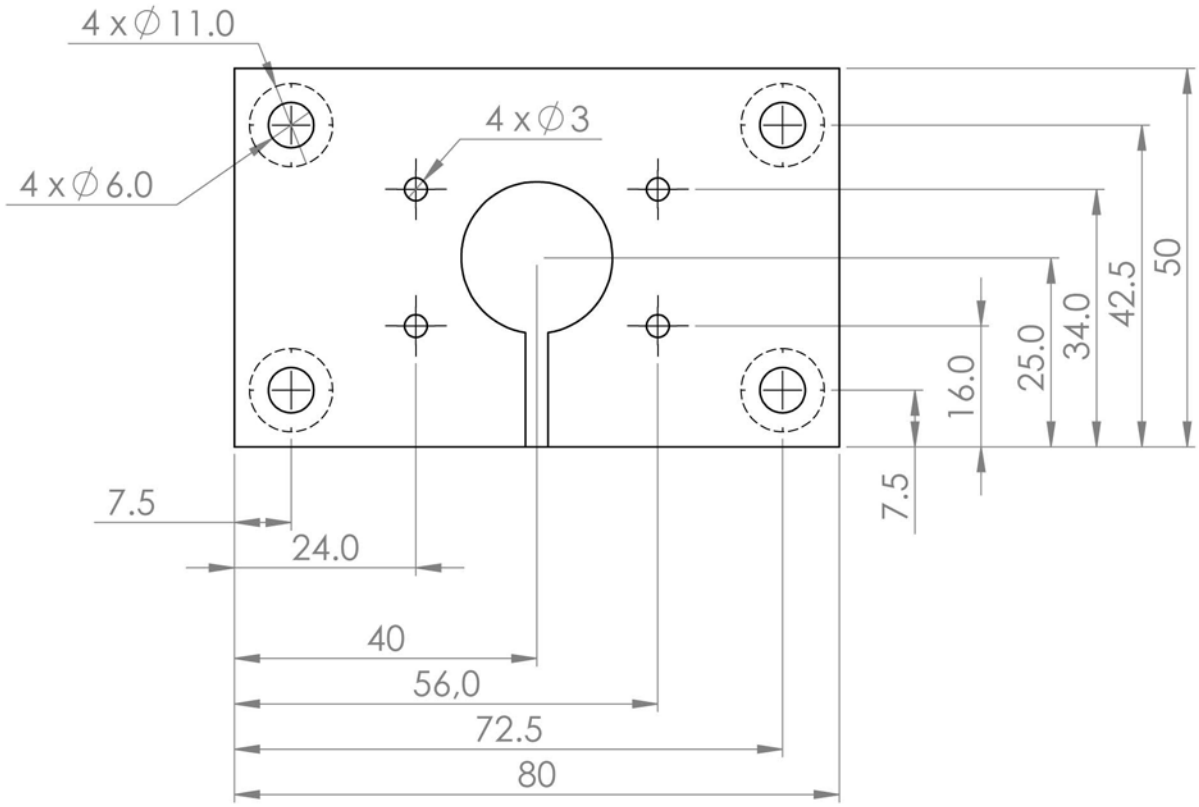

UNLESS OTHERWISE SPECIFIED: DIMENSIONS ARE IN MILLIMETERS SURFACE FINISH: TOLERANCES: LINEAR: ANGULAR:		FINISH:		DEBUR AND BREAK SHARP EDGES	DO NOT SCALE DRAWING	REVISION
	NAME	SIGNATURE	DATE		TITLE:	
DRAWN					Base	
CHK'D						
APPV'D						
MFG						
Q.A				MATERIAL: Steel	DWG NO.	A4
				WEIGHT:	SCALE:1:1	SHEET 1 OF 1

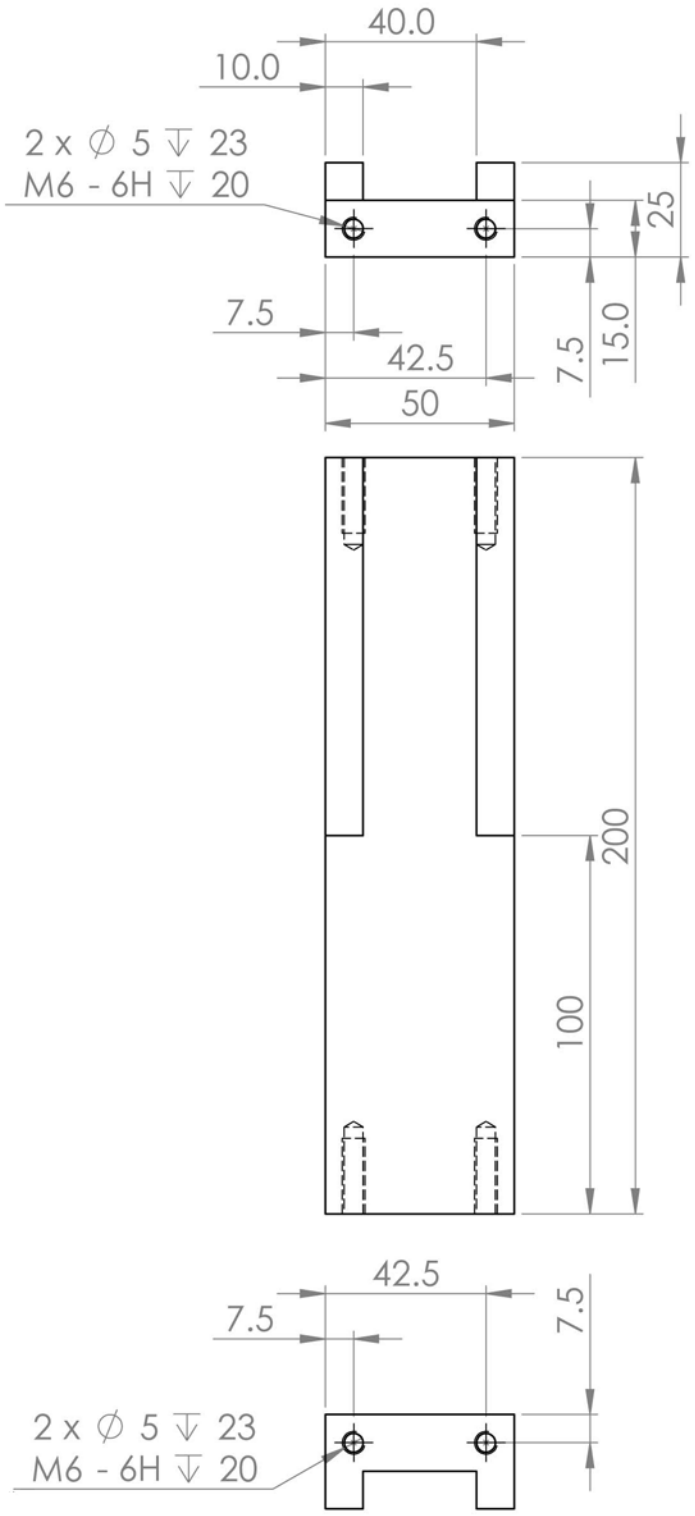

UNLESS OTHERWISE SPECIFIED: DIMENSIONS ARE IN MILLIMETERS SURFACE FINISH: TOLERANCES: LINEAR: ANGULAR:		FINISH:		DEBUR AND BREAK SHARP EDGES	DO NOT SCALE DRAWING	REVISION
	NAME	SIGNATURE	DATE		TITLE:	
DRAWN					Leg	
CHK'D						
APPV'D						
MFG						
Q.A				MATERIAL: Steel	DWG NO.	A4
				WEIGHT:	SCALE:1:2	SHEET 1 OF 1

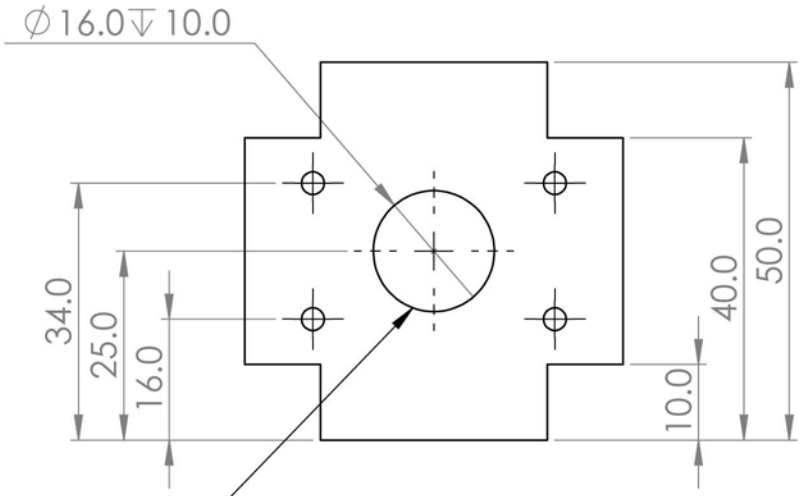

To fit a SUP Ball Bearing F8-16M

- External Diameter = 16 mm
- Bore = 8 mm
- Width = 5 mm

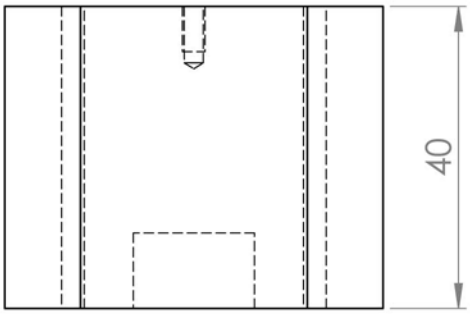

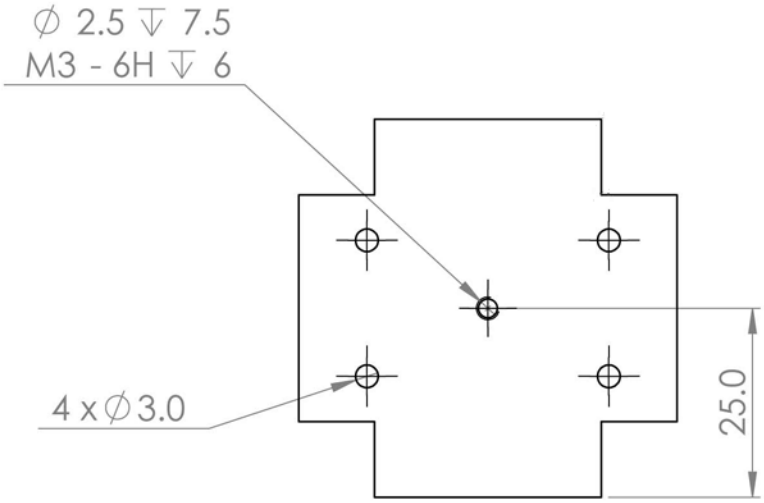

UNLESS OTHERWISE SPECIFIED: DIMENSIONS ARE IN MILLIMETERS SURFACE FINISH: TOLERANCES: LINEAR: ANGULAR:		FINISH:		DEBUR AND BREAK SHARP EDGES	DO NOT SCALE DRAWING	REVISION
	NAME	SIGNATURE	DATE		TITLE:	
DRAWN					Actuator Bearer	
CHK'D						
APPV'D						
MFG						
Q.A				MATERIAL: Steel	DWG NO.	A4
				WEIGHT:	SCALE:1:1	SHEET 1 OF 1

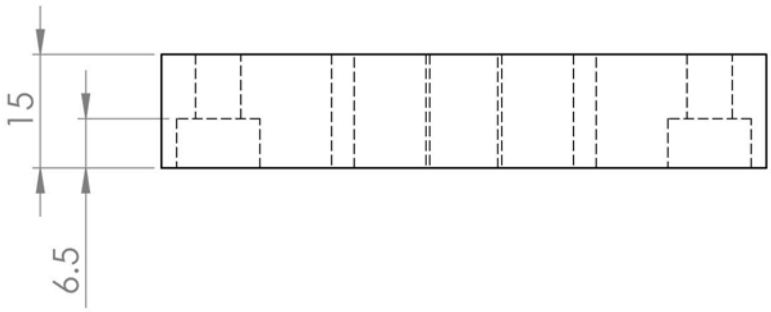

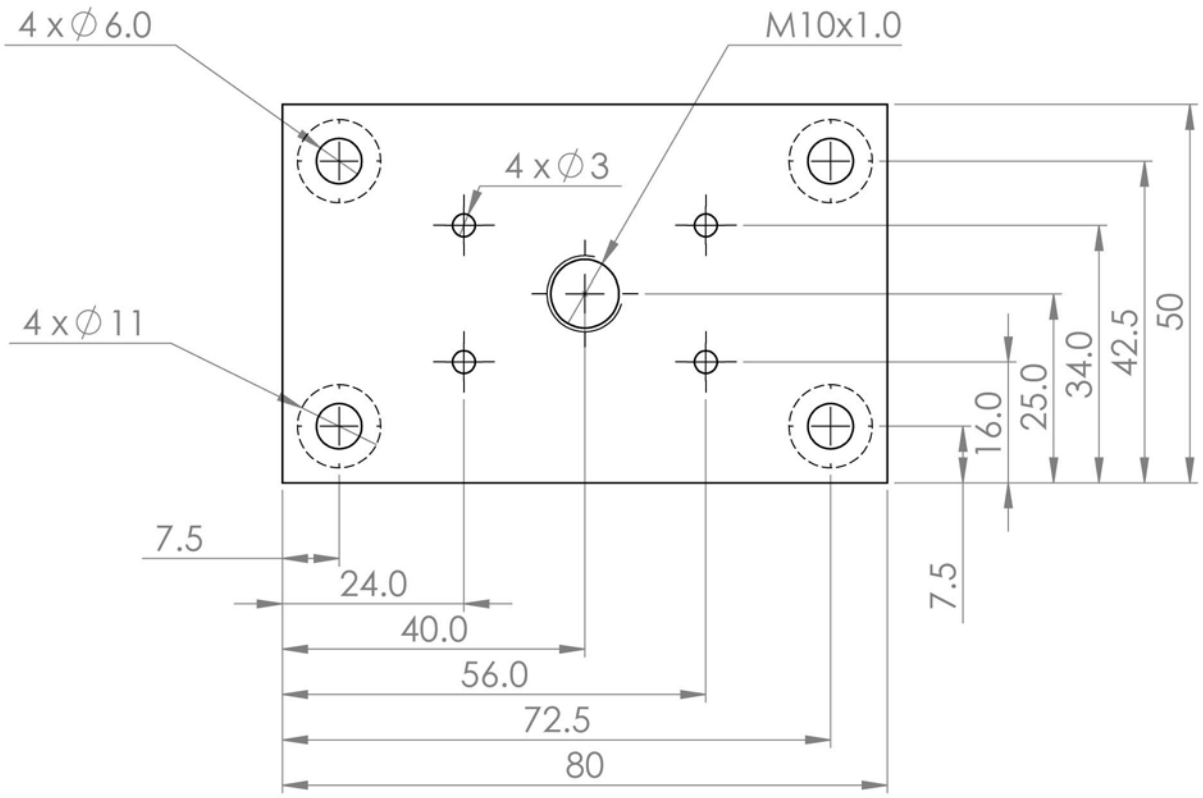

UNLESS OTHERWISE SPECIFIED: DIMENSIONS ARE IN MILLIMETERS SURFACE FINISH: TOLERANCES: LINEAR: ANGULAR:		FINISH:		DEBUR AND BREAK SHARP EDGES	DO NOT SCALE DRAWING	REVISION
	NAME	SIGNATURE	DATE		TITLE:	
DRAWN					Upper Platform	
CHK'D						
APPV'D						
MFG						
Q.A				MATERIAL: Steel	DWG NO.	A4
				WEIGHT:	SCALE:1:2	SHEET 1 OF 1

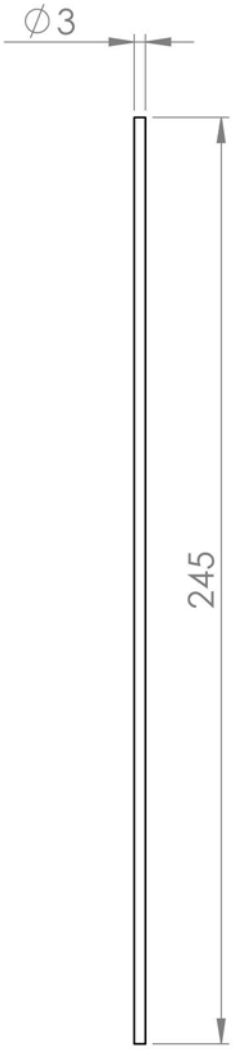

UNLESS OTHERWISE SPECIFIED: DIMENSIONS ARE IN MILLIMETERS SURFACE FINISH: TOLERANCES: LINEAR: ANGULAR:		FINISH:			DEBUR AND BREAK SHARP EDGES	DO NOT SCALE DRAWING / REVISION
	NAME	SIGNATURE	DATE			TITLE: Supporting Rod
DRAWN						
CHK'D						
APPV'D						
MFG						
Q.A				MATERIAL: Steel		DWG NO. / A4
				WEIGHT:		SCALE:1:2 / SHEET 1 OF 1